Article

ADAR1 mutation causes ZBP1-dependent immunopathology

https://doi.org/10.1038/s41586-022-04896-7

Received: 23 September 2021

Accepted: 23 May 2022

Published online: 20 July 2022

Check for updates

Nicholas W. Hubbard[1], Joshua M. Ames[1,3], Megan Maurano[1,3], Lan H. Chu[1], Kim Y. Somfleth[1], Nandan S. Gokhale[1], Margo Werner[1], Jessica M. Snyder[2], Katrina Lichauco[1], Ram Savan[1], Daniel B. Stetson[1] & Andrew Oberst[1]✉

The RNA-editing enzyme ADAR1 is essential for the suppression of innate immune activation and pathology caused by aberrant recognition of self-RNA, a role it carries out by disrupting the duplex structure of endogenous double-stranded RNA species[1,2]. A point mutation in the sequence encoding the Z-DNA-binding domain (ZBD) of ADAR1 is associated with severe autoinflammatory disease[3–5]. ZBP1 is the only other ZBD-containing mammalian protein[6], and its activation can trigger both cell death and transcriptional responses through the kinases RIPK1 and RIPK3, and the protease caspase 8 (refs. [7–9]). Here we show that the pathology caused by alteration of the ZBD of ADAR1 is driven by activation of ZBP1. We found that ablation of ZBP1 fully rescued the overt pathology caused by ADAR1 alteration, without fully reversing the underlying inflammatory program caused by this alteration. Whereas loss of RIPK3 partially phenocopied the protective effects of ZBP1 ablation, combined deletion of caspase 8 and RIPK3, or of caspase 8 and MLKL, unexpectedly exacerbated the pathogenic effects of ADAR1 alteration. These findings indicate that ADAR1 is a negative regulator of sterile ZBP1 activation, and that ZBP1-dependent signalling underlies the autoinflammatory pathology caused by alteration of ADAR1.

ADAR1 modifies endogenous RNAs to prevent activation of the innate immune RNA sensors MDA5, OAS–RNAse L and PKR (refs. [1,2,10,11]). The interferon-inducible p150 isoform of ADAR1 includes an amino-terminal ZBD, and a naturally occurring point mutation in the sequence encoding this region causes a proline-to-alanine substitution at position 193 in human ADAR1 (ref. [4]; Fig. 1a). This mutation is present at a remarkably high rate (about 1 in 360 in individuals of northern European descent), and if paired with a loss-of-function mutation on the second allele of ADAR1, it causes the severe autoinflammatory disease Aicardi–Goutières syndrome[12] (AGS). Recently, a mouse model of this mutation was reported that recapitulates the genetic underpinnings and aspects of the pathology of AGS; mice carrying the mutation causing the P195A substitution (homologous to human P193A) on one or both alleles of *Adar* (which encodes ADAR1) are phenotypically normal, but mice with this mutation combined with deletion of the p150 isoform in the second allele of *Adar* (*Adar*$^{P195A/p150null}$) exhibit liver, kidney and spleen pathology, are runted, and have a median survival of 25 days (ref. [5]).

ZBP1 loss rescues ADAR1 mutation

The *Adar*$^{P195A/p150null}$ model is driven by a point mutation in the sequence encoding the ZBD of ADAR1 (Fig. 1a). As ZBP1 contains the only other mammalian ZBD, we wondered whether these two proteins might functionally interact. Consistent with this possibility, our observations showed that ADAR1 co-immunoprecipitated with ZBP1, but that this interaction was abrogated when point mutations were introduced to the sequence encoding the ZBD of ZBP1 that prevented RNA binding (Extended Data Fig. 1a,b). We also observed that the interaction between ZBP1 and ADAR1 was strengthened by ultraviolet crosslinking, which covalently links protein to nucleic acid (Extended Data Fig. 1c). As these data suggested that ADAR1 and ZBP1 bind a common ligand through their ZBDs, we wondered whether the pathology caused by alteration of the ZBD of ADAR1 in the *Adar*$^{P195A/p150null}$ mouse model was driven by aberrant ZBP1 activation. To test this idea, we crossed *Adar*$^{P195A/p150null}$ mice to mice that lack ZBP1, using a widely used *Zbp1*-knockout mouse strain[13], referred to here as *Zbp1-a* (Fig. 1b). We observed that *Adar*$^{P195A/p150null}$*::Zbp1-a*$^{-/-}$ mice were born at expected frequencies and appeared phenotypically normal (Fig. 1c,d and Extended Data Fig. 2a,b). Following birth, *Adar*$^{P195A/p150null}$*::Zbp1-a*$^{-/-}$ mice gained weight slightly more slowly than *Adar*$^{P195A/WT}$ littermates (Fig. 1e,f), but otherwise exhibited normal phenotype, fertility and survival. The kidney and liver pathology previously reported in *Adar*$^{P195A/p150null}$ mice[5] was also largely normalized by ablation of *Zbp1-a* (Extended Data Fig. 2c).

As we were generating these data, it was reported that the *Zbp1-a*$^{-/-}$ mouse line was not fully congenic to the C57BL/6 genetic background[14], a finding confirmed by our own single nucleotide polymorphism analysis (Extended Data Fig. 3a,b). We therefore generated a second cross of *Adar*$^{P195A/p150null}$ mice to a separately derived, fully congenic *Zbp1*$^{-/-}$ strain[15] referred to here as *Zbp1-g* (Extended Data Fig. 3c). *Adar*$^{P195A/p150null}$

[1]Department of Immunology, University of Washington, Seattle, WA, USA. [2]Department of Comparative Medicine, University of Washington, Seattle, WA, USA. [3]These authors contributed equally: Joshua M. Ames, Megan Maurano. ✉e-mail: oberst@uw.edu

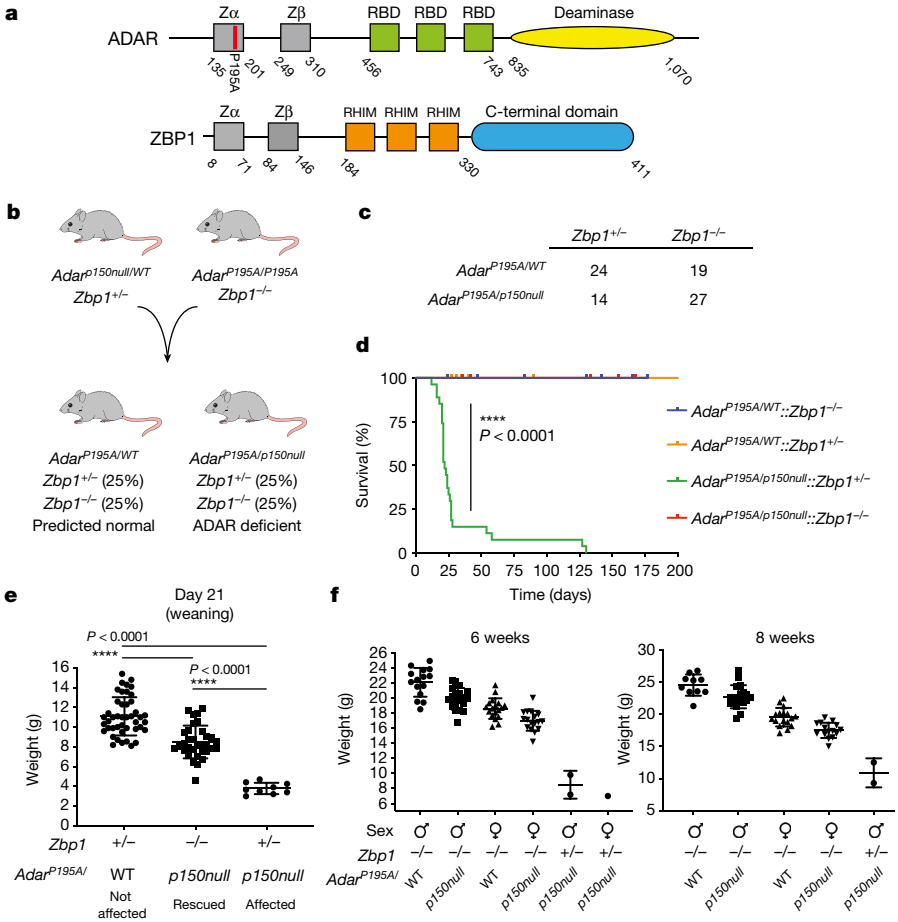

Fig. 1 | Immunopathology in ADAR1-mutant mice is driven by ZBP1. **a**, Schematic of ADAR1 and ZBP1. Zα and Zβ, Z-DNA binding domains; RBD, RNA-binding domain; RHIM, RIP homotypic interaction motif. **b**–**d**, Parental and expected offspring genotypes (**b**), observed genotypes (**c**) and percentage survival for each genotype (**d**) produced by the cross of $Adar^{p150null/WT}$::$Zbp1\text{-}a^{+/-}$ mice to $Adar^{P195A/P195A}$::$Zbp1\text{-}a^{-/-}$ mice. **e**,**f**, Observed weights for mice of the indicated genotypes at 3 (**e**), 6 (**f**, left) and 8 (**f**, right) weeks of age. Survival curves in **d** represent littermates across 18 litters, $Adar^{P195A/WT}$::$Zbp1^{-/-}$ ($n = 19$), $Adar^{P195A/WT}$::$Zbp1^{+/-}$ ($n = 24$), $Adar^{P195A/p150null}$::$Zbp1^{+/-}$ ($n = 14$), $Adar^{P195A/p150null}$::$Zbp1^{-/-}$ ($n = 27$). $^{****}P \leq 0.0001$ (Mantel–Cox log-rank test). For litter weights: $Adar^{P195A/WT}$::$Zbp1^{+/+}$ ($n = 17$), $Adar^{P195A/p150null}$::$Zbp1^{+/+}$ ($n = 18$), $Adar^{P195A/p150null}$::$Zbp1^{+/+}$ ($n = 5$). $^{****}P \leq 0.0001$, unpaired *t*-test, two-tailed. Weights: 6 weeks, from left to right, $n = 15, 19, 18, 17, 2, 1$; 8 weeks, from left to right, $n = 10, 18, 17, 15, 2$. The bars in **e** and **f** represent mean ± s.d.

::$Zbp1\text{-}g^{-/-}$ mice also appeared phenotypically normal (Extended Data Fig. 3d). Notably, we also observed an extension of survival in $Adar^{P195A/p150null}$::$Zbp1\text{-}g^{+/-}$ mice, an effect not observed in $Adar^{P195A/p150null}$::$Zbp1\text{-}a^{+/-}$ mice (Extended Data Fig. 2a). Together, these data confirm that loss of ZBP1 reverses the immunopathology observed in $Adar^{P195A/p150null}$ mice.

Complete ablation of the p150 isoform of ADAR1 causes uniform lethality during embryonic development, but crossing these mice to mice that lack the double-stranded-RNA sensor MDA5 (encoded by *Ifih1*) allows $Adar^{p150null/p150null}$ mice to survive to birth[1]. As MDA5 is a potent inducer of type I interferon (IFN), and because ZBP1 expression is stimulated by IFN (Extended Data Fig. 4a), we reasoned that loss of MDA5 might rescue *Adar-p150* knockout in mice by preventing ZBP1 upregulation. However, in mouse embryonic fibroblasts (MEFs), we observed that although loss of MDA5 completely abrogated IFN production induced by ADAR1 depletion, ZBP1 upregulation was only modestly attenuated (Extended Data Fig. 4b). This suggested that loss of ADAR1 could lead to ZBP1 upregulation and activation even in the absence of MDA5. Consistent with this finding, our observations showed that the survival of $Adar^{p150null/p150null}$::$Ifih1^{-/-}$ mice was modestly but significantly extended by concurrent deletion of ZBP1 (Extended Data Fig. 4c). However, deletion of ZBP1 alone did not allow $Adar^{p150null/p150null}$ mice to survive to birth (Extended Data Fig. 4d). Together, these data indicate that the developmental lethality induced by deletion of ADAR1-p150 is mediated by simultaneous activation of ZBP1, MDA5 and other pathways.

An inflammatory signature remains in rescued mice

$Adar^{P195A/p150null}$ mice exhibit aberrant activation of MDA5, which drives IFN-dependent inflammation. We reasoned that this IFN-dependent signature would still be present in $Adar^{P195A/p150null}$::$Zbp1\text{-}g^{-/-}$ mice, despite their normal phenotype. Consistent with this possibility, RNA-sequencing analysis of spleens from 23-day-old pups revealed that many aspects of the aberrant inflammatory and interferon-stimulated gene (ISG) signature present in $Adar^{P195A/p150null}$ mice were also present in $Adar^{P195A/p150null}$::$Zbp1^{-/-}$ mice, despite them having no alterations in splenic cellularity (Fig. 2a–c, Extended Data Fig. 5a,b and Extended Data Fig. 6). Gene ontology analysis confirmed that the antiviral gene signature induced by alteration of ADAR1 was conserved in $Adar^{P195A/p150null}$::$Zbp1\text{-}g^{-/-}$ mice (Extended Data Fig. 5c). This analysis also identified gene signatures present in $Adar^{P195A/p150null}$ mice but absent in $Adar^{P195A/p150null}$::$Zbp1\text{-}g^{-/-}$ mice (Extended Data Fig. 5d). These genes may indicate targets of ZBP1 signalling or may represent pathways upregulated as a result of the immunopathology present in $Adar^{P195A/p150null}$ mice. In carrying out these analyses, we noted that although cells from $Adar^{P195A/p150null}$::$Zbp1^{-/-}$ mice maintain many aspects of the ISG signature observed in $Adar^{P195A/p150null}$ mice, its magnitude is reduced (Fig. 2c

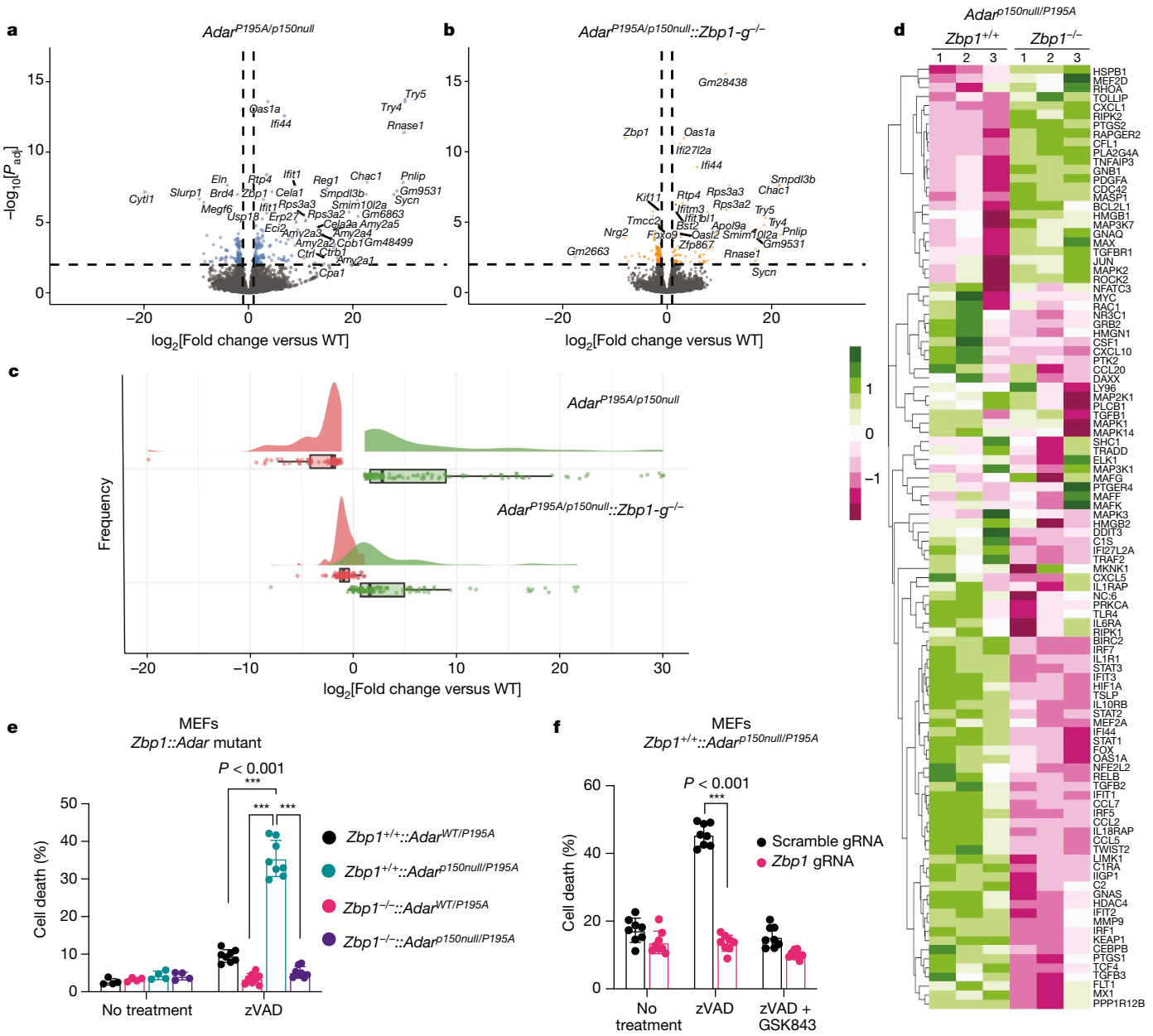

Fig. 2 | The inflammatory program initiated by alteration of ADAR1 remains intact following knockout of *Zbp1*. **a**,**b**, Volcano plots depicting differential expression of genes detected by RNA sequencing of whole spleen tissue derived from 23-day-old mice of the genotypes (**a**) *Adar*$^{P195A/p150null}$ (affected) $n = 4$ (**a**) and *Adar*$^{P195A/p150null}$*::Zbp1-g*$^{-/-}$ (rescued) $n = 5$ (**b**), in each case compared to spleens derived from WT pups ($n = 4$). **c**, Raincloud plots of affected ($n = 4$) and ZBP1 ($n = 5$) rescued mice depicting the statistically significant upregulated and downregulated ADAR1 signature identified in **a**. The ADAR1 signature was identified from the differential analysis of ADAR1 versus WT from genes with a $\log_2$[fold change] > 1 and adjusted *P* value < 0.01. **d**, Heatmap analysis of differential gene expression from NanoString analysis of WT versus *Zbp1*$^{-/-}$ ADAR1-mutant MEFs. Colours denote a row *z*-score (−2 to 2) indicating differential expression of gene counts of indicated genes. **e**,**f**, Cell death, as measured by loss of plasma membrane integrity using an IncuCyte imager, of *Adar*-mutant MEFs after 8 h zVAD treatment on *Adar*::*Zbp1*-mutant MEFs (genetic knockout/mutants) (**e**) or *Adar*-mutant MEFs with CRISPR–Cas9 knockout of *Zbp1* (**f**). GSK843 is an inhibitor of RIPK3. Each experimental group (bar) contains $n = 8$ biological replicates (8 wells). Statistical significance was determined by unpaired Student *t*-tests, two-tailed. Incucyte analyses (**e**,**f**) are single representatives of independently duplicated experiments. Whisker bars (**e**,**f**) represent mean ± s.d.

and Extended Data Fig. 5a). This was confirmed by direct comparison of MEFs isolated from *Adar*$^{P195A/p150null}$ or *Adar*$^{P195A/p150null}$*::Zbp1*$^{-/-}$ mice (Fig. 2d), and suggested that ZBP1 may have a role in augmenting ISG upregulation, a function previously ascribed to ZBP1 in other contexts[16].

We next sought to understand the pathways downstream of ZBP1 that are activated by alteration of ADAR1. We observed that culturing MEFs from *Adar*$^{P195A/p150null}$ mice led to the ZBP1-dependent loss of RIPK3 expression (Extended Data Fig. 7a), suggesting that the ZBP1–RIPK3 pathway is constitutively active in these cells. Consistent with this, our observations showed that despite the reduced level of RIPK3 expression in these cells, treating them with the caspase inhibitor zVAD caused ZBP1-dependent RIPK3 phosphorylation and cell death (Fig. 2e,f and Extended Data Fig. 7a,b). Together, these results indicated that *Adar*$^{P195A/p150null}$ cells are sensitized to ZBP1-dependent necroptosis.

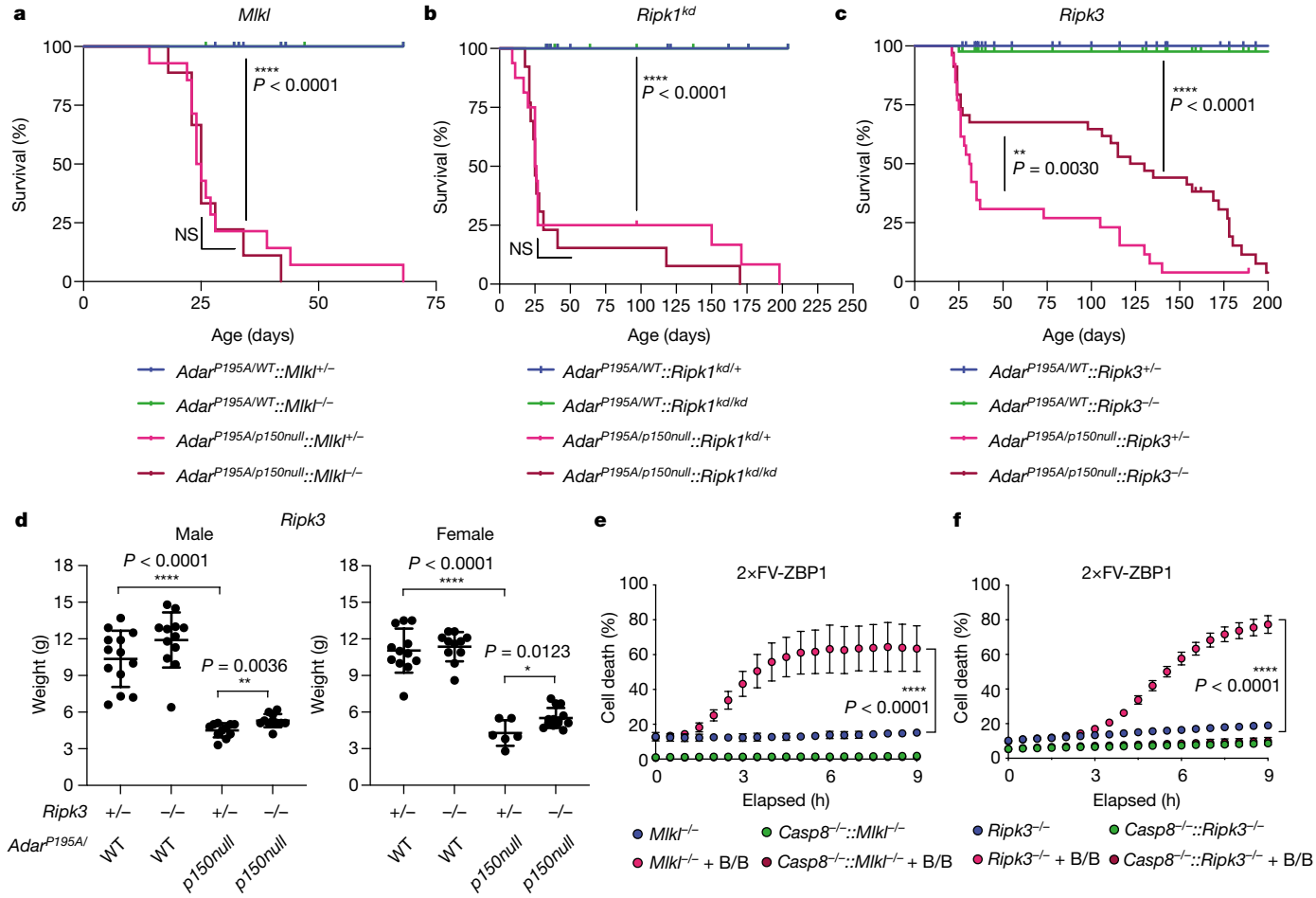

Fig. 3 | ZBP1-induced necroptosis does not underlie immunopathology induced by alteration of ADAR1. a–**c**, Survival proportions for *Adar*$^{P195A/p150null}$ mice crossed to mice that lack MLKL (**a**), carrying a point mutation abrogating the kinase activity of RIPK1 (*Ripk1*^{kd}) (**b**) or lacking RIPK3 (**c**). In each case, the result of a breeding scheme analogous to that depicted in Fig. 1b is shown. Survival proportions (**a**–**c**) represent littermates from 9 (*Mlkl*; **a**), 10 (*Ripk1*$^{kinase\text{-}dead}$ (*Ripk1*^{kd}); **b**) or 18 (*Ripk3*; **c**) litters; *Adar*$^{P195A/WT}$*::Mlkl*$^{+/-}$ ($n = 28$), *Adar*$^{P195A/WT}$*::Mlkl*$^{-/-}$ ($n = 10$), *Adar*$^{P195A/p150null}$*::Mlkl*$^{+/-}$ ($n = 14$), *Adar*$^{P195A/p150null}$*::Mlkl*$^{-/-}$ ($n = 9$); *Adar*$^{P195A/WT}$*::Ripk1*$^{kd/+}$ ($n = 25$), *Adar*$^{P195A/WT}$*::Ripk1*$^{kd/kd}$ ($n = 27$), *Adar*$^{P195A/p150null}$*::Ripk1*$^{kd/+}$ ($n = 16$), *Adar*$^{P195A/p150null}$*::Ripk1*$^{kd/kd}$ ($n = 13$); *Adar*$^{P195A/WT}$*::Ripk3*$^{+/-}$ ($n = 45$), *Adar*$^{P195A/WT}$*::Ripk3*$^{-/-}$ ($n = 42$), *Adar*$^{P195A/p150null}$*::Ripk3*$^{+/-}$ ($n = 26$), *Adar*$^{P195A/p150null}$*::Ripk3*$^{-/-}$ ($n = 34$). Survival statistics determined by log-rank (Mantel–Cox) test; exact *P* values are indicated on the curves. NS, not significant. **d**, Weights of male (left) and female (right) *Ripk3*$^{-/-}$ mice, observed at 21 days after birth. For litter weights: *Adar*$^{P195A/WT}$*::Ripk3*$^{+/-}$ (male/female $n = 13/12$), *Adar*$^{P195A/WT}$*::Ripk3*$^{-/-}$ (male/female $n = 12/11$), *Adar*$^{P195A/p150null}$*::Ripk3*$^{-/-}$ (male/female $n = 11/6$), *Adar*$^{P195A/p150null}$*::Ripk3*$^{+/-}$ (male/female $n = 11/13$). Statistical differences were determined by individual unpaired *t*-tests (two-tailed); exact *P* values are indicated on the plots. **e**,**f**, Cell death, as measured by loss of plasma membrane integrity, observed in MEFs from *Mlkl*$^{-/-}$ and *Mlkl*$^{-/-}$*::Casp8*$^{-/-}$ ($n = 3$ for each group) (**e**) and *Ripk3*$^{-/-}$ and *Ripk3*$^{-/-}$*::Casp8*$^{-/-}$ ($n = 4$ for each group) (**f**) genotypes stably expressing 2×FV-ZBP1, following treatment with the activating drug B/B. The data in **e** and **f** are representative of three independently replicated experiments. Whisker bars (**d**–**f**) represent mean ± s.d.

Cell death signalling in ADAR1 mutant mice

Given this finding, we next sought to address the role of the necroptotic pathway in the pathology of *Adar*$^{P195A/p150null}$ mice. To do this, we crossed *Adar*$^{P195A/p150null}$ mice to mice that lack different components of the necroptotic pathway. Ablation of the necroptotic effector MLKL did not alter the phenotype of *Adar*$^{P195A/p150null}$ mice (Fig. 3a and Extended Data Fig. 8a), nor did crossing them to mice in which the kinase activity of RIPK1 is absent (Fig. 3b and Extended Data Fig. 8b), indicating that prevention of canonical necroptosis alone was not sufficient to explain the effect of *Zbp1* knockout in these mice.

By contrast, ablation of RIPK3 led to a significant extension of survival in *Adar*$^{P195A/p150null}$ mice (Fig. 3c). However, this extension of survival was partial, with approximately one-third of *Adar*$^{P195A/p150null}$*::Ripk3*$^{-/-}$ mice succumbing to death within 40 days of birth, followed by slower attrition of mice over the next 200 days. *Adar*$^{P195A/p150null}$*::Ripk3*$^{-/-}$ were severely runted, in contrast to the overtly normal phenotype observed in *Adar*$^{P195A/p150null}$*::Zbp1*$^{-/-}$ mice (Fig. 3d). These findings indicate that ZBP1 can drive pathology in *Adar*$^{P195A/p150null}$ through signalling that is independent of RIPK3. After influenza infection, ZBP1 was reported to induce RIPK3-dependent induction of both caspase-8-dependent apoptosis and MLKL-dependent necroptosis[17]. Nonetheless, our finding that in *Adar*$^{P195A/p150null}$ mice ablation of RIPK3 failed to fully recapitulate the reversal of pathology observed following ablation of ZBP1 implies RIPK3-independent functions of ZBP1 when activated downstream of ADAR1 deficiency.

ZBP1 contains three confirmed RIP homotypic interaction motifs, which bind to similar domains present in RIPK1 and RIPK3 (ref. [18]). We reasoned that, in the absence of RIPK3, ZBP1 may interact with RIPK1 to scaffold and activate caspase-8-dependent apoptosis. To study this, we turned to a reductive system in which ZBP1 could be directly activated. By replacing the ZBD of ZBP1 with tandem inducible dimerization domains derived from the protein FK506, we created a form of ZBP1 that could be activated using the cell-permeable small molecule B/B (Extended Data Fig. 9a). In wild-type (WT) lung epithelial type 1 (LET1) cells, SV40-transformed endothelial cells (SVECs) or MEFs, this construct

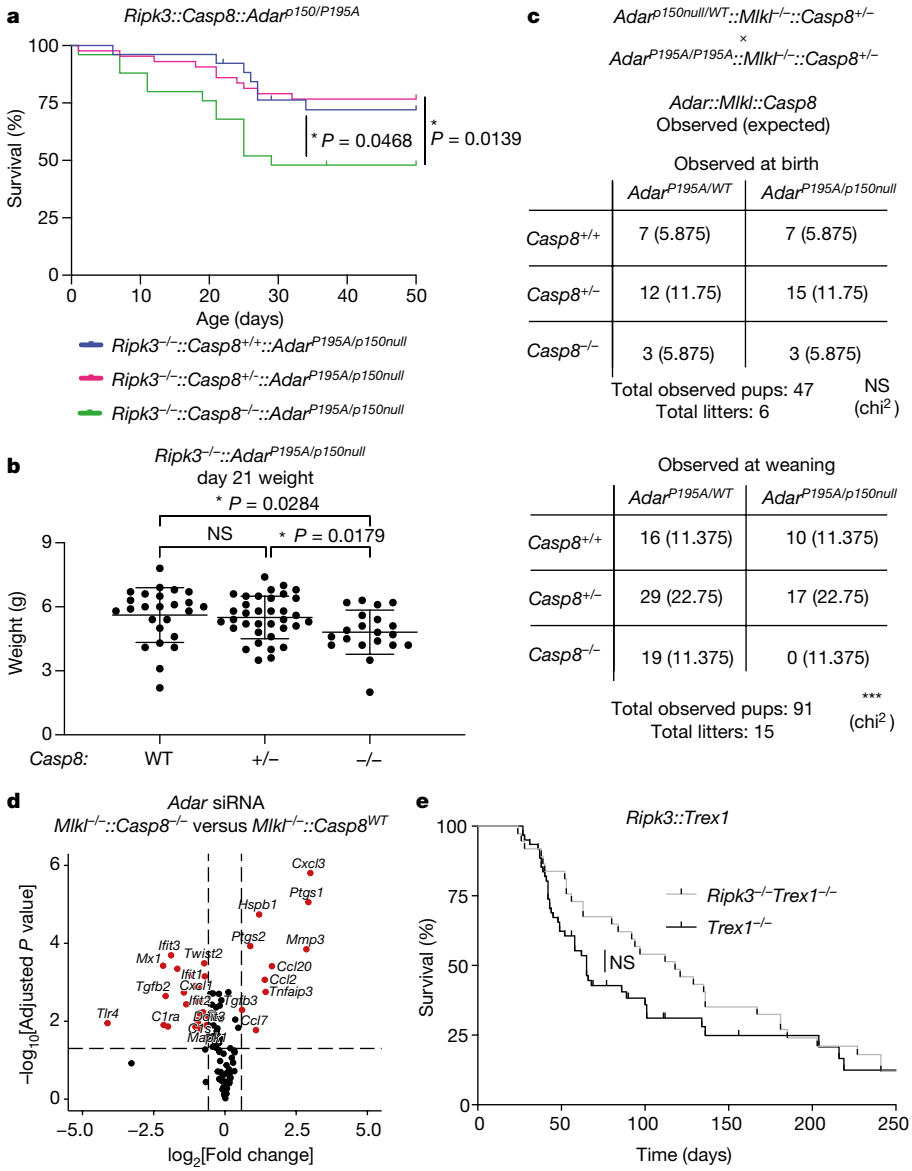

Fig. 4 | Caspase 8 suppresses lethal inflammatory signalling in ADAR1-mutant mice. a,**b**, *Ripk3*$^{-/-}$*::Casp8*$^{-/-}$*::Adar*$^{P195A/p150null}$ cross survival (**a**) and weight (**b**) at weaning (day 21). For **a**, the log-rank (Mantel–Cox) statistical test carried out on survival curves for survival to day 50 between *Ripk3*$^{-/-}$*::Adar*$^{P195A/p150null}$ littermates (*Adar*$^{P195A/WT}$ mice excluded from comparison) that were *Casp8*$^{+/+}$ ($n = 26$), *Casp8*$^{+/-}$ ($n = 43$) and *Casp8*$^{-/-}$ ($n = 25$) showed a significant decrease in the proportion of survival for *Casp8*$^{-/-}$ mice compared to that for *Casp8*$^{+/+}$ ($P = 0.0468$) and *Casp8*$^{+/-}$ ($P = 0.0139$) mice. For **b**, the difference between *Casp8*$^{+/+}$ and *Casp8*$^{+/-}$ was not significant. Individual Student *t*-tests carried out on affected mouse weights (*Adar*$^{P195A/p150null}$) show a statistically significant decrease in *Casp8*$^{-/-}$ ($n = 20$) compared to *Casp8*$^{+/+}$ ($n = 25$), $P = 0.0284$, and *Casp8*$^{+/-}$ ($n = 35$), $P = 0.0179$, mice. **c**, Observed and expected mice from the *Mlkl*$^{-/-}$*::Casp8*$^{-/-}$*::Adar*$^{P195A/p150null}$ cross at birth (day 0) and at weaning (day 21). Chi-square power analysis was carried out on observed/expected frequencies at birth (not significant) and weaning (***$P = 0.000596$). **d**, Volcano plots showing differential gene expression from NanoString analysis of MEFs derived from *Mlkl*$^{-/-}$ or *Mlkl*$^{-/-}$*::Casp8*$^{-/-}$ embryos, following depletion of ADAR1 mediated by short interfering RNA. **e**, Survival proportions for *Trex1*$^{-/-}$ ($n = 61$) and *Trex1*$^{-/-}$*::Ripk3*$^{-/-}$ ($n = 37$) mice. Not significant (Mantel–Cox log-rank test). Whisker bars (**b**) represent mean ± s.d.

(termed 2×FV-ZBP1) triggered cell death that was blocked only with combined inhibition of RIPK3 and the caspases, consistent with induction of both apoptosis and necroptosis downstream of ZBP1 activation (Extended Data Fig. 9b–d). Furthermore, B/B activation of ZBP1 resulted in phosphorylation of RIPK3 and MLKL, and when ZBP1 was directly activated in *Mlkl*$^{-/-}$ MEFs, it induced robust cell death that was dependent on caspase 8 and involved cleavage of caspase 3, consistent with apoptosis (Fig. 3e and Extended Data Fig. 10a,b). ZBP1 activation in *Ripk3*$^{-/-}$ MEFs also induced caspase-8-dependent cell death and caspase 3 cleavage, albeit with slower kinetics than those observed in *Mlkl*$^{-/-}$ cells (Fig. 3e,f). Notably, ZBP1 activation did not trigger detectable cell death in MEFs lacking both MLKL and caspase 8, or both RIPK3 and caspase 8 (Fig. 3e,f). This finding indicates that although RIPK3 can contribute to ZBP1-dependent apoptosis, ZBP1 can still drive caspase-8-dependent cell death responses in the absence of RIPK3.

Caspase 8 suppresses lethal inflammation

We reasoned that cell death dependent on ZBP1, RIPK1 and caspase 8 could underlie the pathology observed in *Adar*$^{P195A/p150null}$*::Mlkl*$^{-/-}$ and *Adar*$^{P195A/p150null}$*::Ripk3*$^{-/-}$ mice. Deletion of caspase 8 causes embryonic lethality due to unrestrained necroptosis[18], but this phenotype is reversed by co-ablation of RIPK3 or MLKL (refs. [19–21]). We therefore generated *Adar*$^{P195A/p150null}$*::Mlkl*$^{-/-}$*::Casp8*$^{-/-}$ and *Adar*$^{P195A/p150null}$

::Ripk3$^{-/-}$*::Casp8*$^{-/-}$ mice to test whether ablation of caspase 8 in addition to necroptotic signalling would recapitulate the phenotypic rescue observed following ablation of ZBP1. Unexpectedly, *Adar*$^{P195A/p150null}$*::Ripk3*$^{-/-}$*::Casp8*$^{-/-}$ mice exhibited reduced weight and survival compared to *Adar*$^{P195A/p150null}$*::Ripk3*$^{-/-}$*::Casp8*$^{+/-}$ littermates (Fig. 4a,b and Extended Data Fig. 10c), whereas *Adar*$^{P195A/p150null}$*::Mlkl*$^{-/-}$*::Casp8*$^{-/-}$ mice were born at expected frequencies but uniformly failed to survive to weaning (Fig 4c). Histological analysis of these mice at birth revealed broadly normal development of the liver and kidney (Extended Data Fig. 11a–c), but a significant increase in IBA1-positive activated microglia in the brains of *Adar*$^{P195A/p150null}$*::Mlkl*$^{-/-}$*::Casp8*$^{-/-}$ neonates, consistent with unrestrained inflammatory signalling at this site (Extended Data Fig. 11d,e). These findings imply that caspase 8 suppresses ZBP1 activation in *Adar*$^{P195A/p150null}$ mice, and that ablation of caspase 8 may allow unrestrained ZBP1 transcriptional signalling that is independent of canonical apoptosis or necroptosis. Consistent with this possibility, co-immunoprecipitation experiments revealed recruitment of RIPK1, or of both RIPK1 and RIPK3, following 2×FV-ZBP1 activation in *Ripk3*$^{-/-}$*::Casp8*$^{-/-}$ or *Mlkl*$^{-/-}$*::Casp8*$^{-/-}$ MEFs, respectively, despite the lack of cell death responses observed in these conditions (Fig 3e,f and Extended Data Fig. 12a,b). We also observed that in *Adar*$^{P195A/p150null}$*::Mlkl*$^{-/-}$ MEFs, zVAD treatment stabilized the interaction between ZBP1 and RIPK3, again in the absence of cell death responses (Extended Data Fig. 12c). These findings indicate that when necroptotic effectors are absent, loss or inhibition of caspase 8 promotes interactions between ZBP1 and the RIP kinases.

We next assessed whether loss of caspase 8 potentiated transcriptional signalling induced by ADAR1 insufficiency. We observed that whereas depletion of ADAR1 mediated by short interfering RNA in *Mlkl*$^{-/-}$ cells induced the expected upregulation of ISGs, ADAR1 depletion in *Mlkl*$^{-/-}$*::Casp8*$^{-/-}$ MEFs induced a distinct transcriptional response dominated by NF-κB targets (Fig. 4d and Extended Data Fig. 13a,b). As RIPK1 is a key signalling adapter upstream of NF-κB activation[22], this finding implied that ZBP1–RIPK1 signalling may underlie these transcriptional effects. Consistent with this, our observations showed that 2×FV-ZBP1 activation in *Mlkl*$^{-/-}$ MEF s induced RIPK1-dependent upregulation of the NF-κB targets CCL2 and CCL7, but not of the canonical ISG IFIT1 (Extended Data Fig. 13c). Together, these data indicate that following alteration or depletion of ADAR1, caspase 8 acts to suppress a ZBP1- and RIPK1-dependent program of inflammatory transcription. The modest extension of survival observed in *Adar*$^{P195A/p150null}$*::Ripk3*$^{-/-}$*::Casp8*$^{-/-}$ mice relative to *Adar*$^{P195A/p150null}$*::Mlkl*$^{-/-}$*::Casp8*$^{-/-}$ mice suggests that RIPK3 can potentiate, but is not required for, ZBP1- and RIPK1-dependent inflammatory signalling.

This study does not address the identity of the ligand(s) responsible for activating ZBP1 in *Adar*$^{P195A/p150null}$ mice. As the P195A alteration in ADAR1 lies in its ZBD, we can speculate that ADAR1(P195A) may be attenuated in its ability to bind ZBD ligands. Interestingly, aligning the ZBD sequences of ADAR1 and ZBP1, along with those present in the fish PKR homologue PKZ (ref. [23]) and the vaccinia virus effector E3L (ref. [24]), reveals that ZBP1 naturally contains an alanine at position 64, the site homologous to P195 of ADAR1 (Extended Data Fig. 14a). As substitution of alanine for proline at this site in ADAR1 limits its function, we speculate that the presence of an alanine at the homologous site within ZBP1 may reflect a naturally lower affinity for ligand by ZBP1 relative to other ZBDs. This may represent a means to limit aberrant ZBP1 activation at steady state. We sought to test this idea by creating a mouse line with a 'revertant' ZBP1, in which A64 is mutated to proline. However, ZBP1(A64P) mice did not reveal evidence of increased ZBP1 activation, either when crossed to the *Adar*$^{P195A/p150null}$ model or in response to influenza infection, but rather seemed attenuated in their signalling in both settings (Extended Data Fig. 14b,c). Although ZBP1(A64P) protein was properly expressed (Extended Data Fig. 14d), this attenuation may reflect a disruption of protein structure induced by this alteration, and implies that further alterations or larger domain swaps would be needed to effectively test this hypothesis. Future studies will clarify the identity of ZBP1 ligands that emerge following alteration of ADAR1.

AGS refers to a family of IFN-driven congenital pathologies driven by alterations in proteins involved in nucleotide sensing and regulation[12]. As ZBP1 is strongly induced by IFN, and has been described to bind DNA as well as RNA[16], we wondered whether ZBP1 and RIPK3 signalling might have a role in AGS-like pathology driven by endogenous DNA ligands. To test this, we assessed mice lacking TREX1, a DNA exonuclease whose ablation causes aberrant activation of the cGAS–STING pathway[25,26]. However, we did not observe significant amelioration of pathology or extension of survival in *TrexI*$^{-/-}$ mice when RIPK3 was ablated, unlike the partial rescue observed in *Adar*$^{P195A/p150null}$ mice following knockout of *Ripk3* (Figs. 4e and 3c). This suggests that engagement of the ZBP1–RIP kinase pathway is a feature of dysregulated endogenous RNA, but not DNA, sensing.

The unexpected susceptibility of *Ripk3*$^{-/-}$*::Casp8*$^{-/-}$ and *Mlkl*$^{-/-}$*::Casp8*$^{-/-}$ mice to alteration of ADAR1 indicates that although these mice develop normally, they are poised for hyperactive inflammatory signalling in response to ZBP1 activation. Indeed, previous studies have found that *Mlkl*$^{-/-}$*::Fadd*$^{-/-}$ mice (comparable to *Mlkl*$^{-/-}$*::Casp8*$^{-/-}$) are highly susceptible to influenza infection[8], a setting in which ZBP1 is strongly activated. Although this was interpreted as indicating a requirement for functional cell death pathways for antiviral defence, our data raise the possibility that these mice succumb to uninhibited inflammatory signalling triggered by ZBP1. Notably, we did not observe engagement of pyroptotic cell death following ZBP1 activation in cells lacking caspase 8 in combination with RIPK3 or MLKL, although our data do not rule out contribution of pyroptotic signalling to the immunopathology we observe.

Our findings identify ZBP1 as a key effector of autoinflammatory pathology induced by alteration of the Z-DNA-binding domain of ADAR1. Our data also highlight the pleiotropic nature of ZBP1 signalling: whereas ZBP1 ablation fully rescued the pathology of the *Adar*$^{P195A/p150null}$ model, individual deletion of the necroptotic signalling molecules MLKL or RIPK3 did not, and ablation of caspase 8 unleashed a lethal inflammatory program, apparently in the absence of ZBP1-dependent programmed cell death. These findings are consistent with the dual functions of caspase 8 as both an inducer of cell death and a suppressor of ZBP1-dependent necroptosis and inflammation. Indeed, both the presence and the absence of caspase 8 may drive pathology in ADAR1-mutant mice. Our in vitro data indicate that ZBP1 activation in the absence of RIPK3 can induce caspase-8-dependent cell death, and this pathway may contribute to the pathology of *Adar*$^{P195A/p150null}$*::Ripk3*$^{-/-}$ mice; conversely, further ablation of caspase 8 in these mice exacerbates the observed pathology by instead unleashing unrestrained inflammatory signalling. Ultimately, apoptosis, necroptosis and inflammatory transcription may all contribute to the pathology of *Adar*$^{P195A/p150null}$ mice, and which of these pathways is engaged following alteration of ADAR1 probably varies between tissues and cell types depending on the abundance of the pathway components as well as of regulatory proteins such as cFLIP and the IAPs. This pleiotropy also suggests that even the combined targeting of apoptosis and necroptosis using small-molecule inhibitors is unlikely to reverse AGS pathology driven by alteration of ADAR1.

Online content

Any methods, additional references, Nature Research reporting summaries, source data, extended data, supplementary information, acknowledgements, peer review information; details of author contributions and competing interests; and statements of data and code availability are available at https://doi.org/10.1038/s41586-022-04896-7.

1. Pestal, K. et al. Isoforms of RNA-editing enzyme ADAR1 independently control nucleic acid sensor MDA5-driven autoimmunity and multi-organ development. *Immunity* **43**, 933–944 (2015).

2. Ahmad, S. et al. Breaching self-tolerance to Alu duplex RNA underlies MDA5-mediated inflammation. *Cell* **172**, 797–810 (2018).
3. Herbert, A. et al. A Z-DNA binding domain present in the human editing enzyme, double-stranded RNA adenosine deaminase. *Proc. Natl Acad. Sci. USA* **94**, 8421–8426 (1997).
4. Rice, G. I. et al. Mutations in *ADAR1* cause Aicardi-Goutières syndrome associated with a type I interferon signature. *Nat. Genet.* **44**, 1243–1248 (2012).
5. Maurano, M. et al. Protein kinase R and the integrated stress response drive immunopathology caused by mutations in the RNA deaminase ADAR1. *Immunity* **54**, 1948–1960 (2021).
6. Schwartz, T., Behlke, J., Lowenhaupt, K., Heinemann, U. & Rich, A. Structure of the DLM-1–Z-DNA complex reveals a conserved family of Z-DNA-binding proteins. *Nat. Struct. Mol. Biol.* **8**, 761–765 (2001).
7. Rebsamen, M. et al. DAI/ZBP1 recruits RIP1 and RIP3 through RIP homotypic interaction motifs to activate NF-κB. *EMBO Rep.* **10**, 916–922 (2009).
8. Thapa, R. J. et al. DAI senses influenza A virus genomic RNA and activates RIPK3-dependent cell death. *Cell Host Microbe* **20**, 674–681 (2016).
9. Upton, J. W., Kaiser, W. J. & Mocarski, E. S. DAI/ZBP1/DLM-1 complexes with RIP3 to mediate virus-induced programmed necrosis that is targeted by murine cytomegalovirus vIRA. *Cell Host Microbe* **11**, 290–297 (2012).
10. Chung, H. et al. Human ADAR1 prevents endogenous RNA from triggering translational shutdown. *Cell* **172**, 811–824 (2018).
11. Li, Y. et al. Ribonuclease L mediates the cell-lethal phenotype of double-stranded RNA editing enzyme ADAR1 deficiency in a human cell line. *Elife* **6**, e25687 (2017).
12. Crow, Y. J. et al. Characterization of human disease phenotypes associated with mutations in *TREX1*, *RNASEH2A*, *RNASEH2B*, *RNASEH2C*, *SAMHD1*, *ADAR*, and *IFIH1*. *Am. J. Med. Genet. A* **167**, 296–312 (2015).
13. Ishii, K. J. et al. TANK-binding kinase-1 delineates innate and adaptive immune responses to DNA vaccines. *Nature* **451**, 725–729 (2008).
14. Koehler, H. S., Feng, Y., Mandal, P. & Mocarski, E. S. Recognizing limits of Z-nucleic acid binding protein (ZBP1/DAI/DLM1) function. *FEBS J.* **287**, 4362–4369 (2020).
15. Newton, K. et al. RIPK1 inhibits ZBP1-driven necroptosis during development. *Nature* **540**, 129–133 (2016).
16. Takaoka, A. et al. DAI (DLM-1/ZBP1) is a cytosolic DNA sensor and an activator of innate immune response. *Nature* **448**, 501–505 (2007).
17. Nogusa, S. et al. RIPK3 activates parallel pathways of MLKL-driven necroptosis and FADD-mediated apoptosis to protect against influenza A virus. *Cell Host Microbe* **20**, 13–24 (2016).
18. Varfolomeev, E. E. et al. Targeted disruption of the mouse caspase 8 gene ablates cell death induction by the TNF receptors, Fas/Apo1, and DR3 and is lethal prenatally. *Immunity* **9**, 267–276 (1998).
19. Oberst, A. et al. Catalytic activity of the caspase-8–$FLIP_L$ complex inhibits RIPK3-dependent necrosis. *Nature* **471**, 363–367 (2011).
20. Kaiser, W. J. et al. RIP3 mediates the embryonic lethality of caspase-8-deficient mice. *Nature* **471**, 368–372 (2011).
21. Alvarez-Diaz, S. et al. The pseudokinase MLKL and the kinase RIPK3 have distinct roles in autoimmune disease caused by loss of death-receptor-induced apoptosis. *Immunity* **45**, 513–526 (2016).
22. Najjar, M. et al. RIPK1 and RIPK3 kinases promote cell-death-independent inflammation by Toll-like receptor 4. *Immunity* **45**, 46–59 (2016).
23. Rothenburg, S. et al. A PKR-like eukaryotic initiation factor 2α kinase from zebrafish contains Z-DNA binding domains instead of dsRNA binding domains. *Proc. Natl Acad. Sci. USA* **102**, 1602–1607 (2005).
24. Koehler, H. et al. Vaccinia virus E3 prevents sensing of Z-RNA to block ZBP1-dependent necroptosis. *Cell Host Microbe* **29**, 1266–1276 (2021).
25. Gray, E. E., Treuting, P. M., Woodward, J. J. & Stetson, D. B. Cutting edge: cGAS is required for lethal autoimmune disease in the Trex1-deficient mouse model of Aicardi–Goutières syndrome. *J. Immunol.* **195**, 1939–1943 (2015).
26. Gall, A. et al. Autoimmunity initiates in nonhematopoietic cells and progresses via lymphocytes in an interferon-dependent autoimmune disease. *Immunity* **36**, 120–131 (2012).

Methods

Mice

Mouse strains with modifications to *Zbp1-a* (ref. [13]), *Zbp1-g* (ref. [15]), *Adar*$^{P195A/p150null}$ (ref. [5]), *Mlkl* (ref. [27]), *Ripk1*^{kd} (ref. [28]), *Ripk1*^{mutRHIM} (ref. [29]), *Ripk3* (ref. [30]) and *Casp8* (refs. [19,31]), *Trex1* (ref. [26]) and *Ifih1* (MDA5) (ref. [1]) have been described previously. *Zbp1*^{A64P} mice were generated as previously described[32], using the single-guide RNA (gRNA) target sequence CCGCCTATGCTCCATGTTGCAGG and the repair-template sequence5′-AAAACCCTCAATCAAGTCCTTTACCGCCTGAAGAAGGAGG ACAGAGTGTCCTCCCCA GAGCCTCCAACATGGAGCATAGGCGG GGCTGCTTCTGGAGATGGGGCTCCTGCAATCCCTGAGAACTCCAGT-3′. In brief, C57BL6/J oocytes were microinjected with Cas9 complexed with a single gRNA and single-stranded-DNA donor template as described, and then implanted into pseudopregnant female mice. Founder pups were screened using the Surveyor assay, and resulting mice were bred to homozygosity and genotyped using a Taqman probe system to detect the *Zbp1*^{A64P} G>C nucleotide change using the primer sequences 5′-CCTCAATCAAGTCCTTTACC-3′ (sense) and 5′-GACAGATTACCAAGGCTAGG-3′ (antisense), 5′-CAGAGCCTGCAACATGGAG-3′ (WT probe) and 5′-CAGAGCCT CCAACATGGAG-3′ (mutant probe). All mice were housed in pathogen-free facilities at the University of Washington under 12-h light–dark cycles with access to food and water ad libitum. Temperatures were set to 74 ± 2 °F with humidity of 30–70%. All animals used were cared for and used in experiments approved by the University of Washington Institutional Animal Care and Use Committee (under protocols 4298-01 and 4190-01) in a facility accredited by the Association for Assessment and Accreditation of Laboratory Animal Care in accordance with the Guide for the Care and Use of Laboratory Animals and applicable laws and regulations. In breeding experiments, no specific criteria were used to determine final sample size. These experiments were not randomized or blinded.

Analysis through single nucleotide polymorphism typing of *Zbp1-a* and *Zbp1-g* mouse strains was carried out by Taconic Biosciences using the Mouse Genome Scan Panel.

Cell lines

MEFs were generated from pups at embryonic day 15 and immortalized by retroviral transduction of the SV40 large T antigen. HEK293T cells, LET1 cells and MEFs were maintained in standard conditions: Dulbecco's modified Eagle medium supplemented with 10% fetal bovine serum, glutamine, penicillin and streptomycin. Following isolation and immortalization, MEF lines were tested for cell death competence by stimulation with TNF/zVAD (RIPK3/RIPK1-dependent cell death) or infection with influenza A virus (ZBP1/RIPK3-dependent cell death).

Plasmids, lentiviral vectors and short interfering RNA

2×FV-ZBP1 was generated by replacing the first 146 amino acids of mouse ZBP1 (corresponding to the ZBD) with tandem copies of FKBP(F36V), from Clontech. The resulting fusion gene was cloned into the Tet-based inducible expression pSLIK vector[33], and this construct was used to create lentiviral particles for transduction of target lines using standard protocols. Expression and activation of this construct were achieved by inducing 2×FV-ZBP1 expression with 1 μg ml^{-1} doxycycline for 12 h, and then treating with 100 mM B/B homodimerizer (Clontech). The full ADAR1-p150 isoform was cloned from mouse cDNA directly into a pRRL lentiviral backbone and subsequently sequenced to confirm identity. WT and mutant Zαβ (mZαβ) ZBP1 were subcloned from constructs previously obtained from the laboratory of Jason Upton into the pRRL backbone, at which point a 3×Flag tag was added to the carboxy terminus.

CRISPR–Cas9-mediated deletion was achieved using a lenti-CRISPR construct created by D. Stetson[5], into which guide sequences listed below were inserted. These were used to create VSV-G-pseudotyped lentivirus particles, which were used to transduce target cells. Following 10–14 days of antibiotic selection, deletion of target proteins was confirmed by western blot. The sequences of the guide RNA (gRNA) target sites are as follows: non-targeting control gRNA: scramble gRNA: 5′-GACGGAGGCTAAGCGTCGCAA-3′, *Zbp1* gRNA: 5′-GAGCCTGCAACATGGAGCAT-3′, *Ifih1* (MDA5) gRNA: 5′-GTGTGGGTTTGACATAGCGCG-3′.

Short interfering RNA (siRNA) experiments were carried out by transfecting cells with SMARTpool siRNA cocktails (Dharmacon Horizon Discovery) targeting ADAR1 (siGenome mouse *Adar*, Entrez Gene 56417), RIPK1 (siGenome mouse *Ripk1*, Entrez Gene 19766) or a non-targeting scramble control (siGenome Non-targeting siRNA Pool 1). Transfection of siRNA was carried out using the dharmaFECT 1 transfection reagent (catalogue number T-2001-03, Horizon Discovery) according to the manufacturer's protocols.

Antibodies and inhibitors

Where indicated, the following drugs were used at the listed concentrations: 50 μM zVAD (SM Biochemicals); 100 nM GSK843 (GlaxoSmithKline).

The following antibodies were used for western blots and immunoprecipitations: ADAR1 (15.8.6, SantaCruz), ZBP1 (Zippy-1, AdipoGen), actin (13E5, Cell Signaling Technology), MDA5 (D74E4, Cell Signaling Technologies), pRIPK3 (GEN135-35-9, Genentech), RIPK3 (1G6.1.4, Genentech or 2283, ProSci), pMLKL (D6E3G, Cell Signaling Technologies), MLKL (MABC604, Millipore), caspase 3 (9662, Cell Signaling Technologies), cleaved caspase 3 (9661, Cell Signaling Technologies), RIPK1 (38/RIP, BD Biosciences), anti-Flag (M2, Sigma) and anti-FKBP12 (PA1-026A, Thermo Fisher). IBA1 (catalogue number 019-19741, Wako-Chem) and cleaved caspase 3 (clone D3E9, Cell Signaling Technologies) were used in immunohistochemical analysis.

The following antibodies were used for flow cytometry analysis of splenocytes: FITC anti-CD19 (clone 1D3, BD Biosciences), PerCP–Cy5.5 anti-CD3e (clone 145-2C11, BD Biosciences), PE–Cy7 anti-Ly6C (clone HK1.4, Biolegend), APC anti-F4/80 (clone BM8, eBioscience), AF700 anti-Ly6G (clone 1A8, Biolegend), APC–Cy7 anti-NK1.1 (clone PK136, BD Biosciences), BV510 anti-CD8a (clone 53-6.7, BD Biosciences), BV605 anti-CD4 (clone RM4-5, BD Biosciences), BV650 anti-CD11b (clone M1/70, Biolegend) and BUV395 anti-CD45.2 (clone 104, BD Biosciences).

Western blot, immunoprecipitation and infrared crosslinking and immunoprecipitation

WT HEK293T cells or HEK293T cells expressing Flag–ZBP1 or Flag–ZBP1 mZαβ were cultured in 6-well plates and were transfected with pRRL vector expressing ADAR1-p150 or empty pRRL vector using ×2 transfection reagent (Mirus). At about 24 h post-transfection, cells were washed in PBS and crosslinked with 254 nm ultraviolet C light (0.3 J cm^{-2}) or left uncrosslinked, and lysed in 200 μl immunoprecipitation lysis buffer (25 mM Tris pH 7.5, 150 mM NaCl, 1% Triton X-100, 0.5 mM EDTA, 5 mM $MgCl_2$ + 1× protease inhibitor). Lysates were clarified by centrifugation at 5,000*g* for 10 min at 4 °C, and quantified by Bradford assay. A fraction of each sample was stored for input controls. A 200 μg quantity of each lysate was incubated with Protein G Dynabeads (Thermo Fisher) pre-conjugated with 4 μg anti-Flag M2 antibody (Sigma) in a final volume of 500 μl immunoprecipitation lysis buffer for 2 h at 4 °C with rotation. The beads were then washed four times with 1 ml immunoprecipitation lysis buffer before boiling them in 2× Laemmli buffer (Bio-Rad) + 5% beta-mercaptoethanol to elute protein complexes. Eluates and input controls were resolved on a 4–15% TGX gel (Bio-Rad) for SDS–polyacrylamide gel electrophoresis, and transferred to polyvinylidene difluoride membranes. Immunoblotting was carried out using horseradish-peroxidase-conjugated anti-Flag and anti-β-actin antibodies, and with anti-ADAR1 primary antibody and horseradish-peroxidase-conjugated anti-mouse secondary antibody (Jackson Immunolabs).

For RIPK3 and RIPK1 immunoprecipitations, Cells were lysed in ice-cold lysis buffer (25 mM Tris-HCl pH 7.4, 150 mM NaCl, 1% v/v Triton X-100, 10% v/v glycerol and 0.01% w/v SDS) supplemented with 1× complete Protease Inhibitor (Roche) for 30 min, followed by centrifugation at 1,000*g* for 10 min. Antibodies to ZBP1 or FKBP12 (Invitrogen, PA1-026A) were immobilized to Dynabeads Protein G (Invitrogen) as per the manufacturer's instructions, and then incubated with total cell lysates overnight at 4 °C. Immunoprecipitates were eluted in Laemmli sample buffer (63 mM Tris-HCl, pH 8.0, 10% v/v glycerol, 2% w/v SDS, 0.01% w/v bromophenol blue, 2.5% v/v 2-mercaptoethanol) at 95 °C for 10 min.

We carried out infrared crosslinking and immunoprecipitation (irCLIP) as described previously[34] with slight modifications. WT HEK293T cells or HEK293T cells stably expressing Flag–ZBP1 or Flag–ZBP1 mZαβ were cultured in 6-well plates. Cells were washed with PBS, crosslinked with 254 nm ultraviolet C light (0.3 J cm^{-2}) and lysed in 200 µl irCLIP lysis buffer (50 mM Tris pH 7.5, 150 mM NaCl, 1 mM EDTA, 1% Triton X-100, 0.1% SDS, 1× protease inhibitor). After sonication in ice slurry, lysates were clarified by centrifugation at 5,000*g* for 10 min at 4 °C, and quantified by Bradford assay (Bio-Rad). A fraction of each sample was stored for input controls. A 200 µg quantity of each lysate was incubated with Protein G Dynabeads (Thermo Fisher) pre-conjugated with 4 µg anti-Flag M2 antibody (Sigma) in a final volume of 500 µl irCLIP lysis buffer for 2 h at 4 °C with rotation. The beads were then sequentially washed with the following ice-cold buffers: once with 1 ml irCLIP lysis buffer, once with 1 ml high-stringency buffer (20 mM Tris pH 7.5, 120 mM NaCl, 25 mM KCl, 5 mM EDTA, 1% Triton X-100, 1% NaDOC, 0.1% SDS), once with 1 ml high-salt buffer (20 mM Tris pH 7.5, 500 mM NaCl, 5 mM EDTA, 1% Triton X-100, 1% NaDOC), once with 1 ml low-salt buffer (20 mM Tris pH 7.5, 5 mM NaCl, 5 mM EDTA, 1% Triton X-100) and twice with 0.5 ml NT2 buffer (50 mM Tris pH 7.5, 150 mM NaCl, 1 mM $MgCl_2$, 0.05% NP-40). Beads were then resuspended in 30 µl NT2 buffer containing 25 ng ml^{-1} RNase A (Thermo Fisher) and 15% PEG400 (Sigma) for on-bead RNase digestion at 30 °C for 15 min with shaking (1,200 r.p.m.) in a Thermomixer. RNase digestion was quenched by the addition of 0.5 ml high-stringency buffer. Beads were washed twice with 0.3 ml PNK wash buffer (50 mM Tris pH 7.0, 10 mM $MgCl_2$), and then resuspended in 30 µl PNK dephosphorylation mix (1× PNK buffer (Promega), 0.5 µl RNaseIN (Promega), 1 µl T4 PNK (Promega), 4 µl PEG400). Dephosphorylation reactions were conducted at 37 °C for 60 min with shaking (1,200 r.p.m.) in a Thermomixer. Dephosphorylation mix was removed and beads were washed with 0.25 ml PNK wash buffer. For ligation of oligonucleotide conjugated with infrared dye to protein-crosslinked RNA, beads were resuspended in 30 µl RNA ligation mix (1× RNA ligase I buffer (NEB), 1 µl RNA ligase I (NEB), 1 µl infrared-dye-labelled oligonucleotide[34], 5 µl PEG400 and 0.5 µl RNaseIN) and incubated for 16 h at 16 °C with shaking in a Thermomixer (1,200 r.p.m.). The ligation mix was then removed, and the beads were washed twice with 0.25 ml PNK wash buffer, before elution of RNA–protein complexes in 20 µl 1× LDS Buffer (Thermo Fisher) + 10% beta-mercaptoethanol at 80 °C for 10 min. A 5 µl volume of eluates, as well as input controls, was then resolved by SDS–polyacrylamide gel electrophoresis on 4–12% Bis-Tris NuPAGE gels (Thermo Fisher), and transferred to nitrocellulose membranes. Fluorescent RNA–protein complexes in the eluates were visualized on a LiCOR Odyssey FC imager.

Flow cytometry

Splenocytes were blocked with Fc block (BD Biosciences) in PBS + 2% heat-inactivated fetal bovine serum for 10 min at 4 °C before cell surface staining by subsequent addition of a pre-mixed antibody cocktail. Cells were incubated with fluorescently labelled antibodies, each at a dilution of 1:200 for 30 min at 4 °C, washed and fixed with 2% paraformaldehyde in PBS for 10 min. Data were acquired on a BD FACSymphony A3 Cell Analyzer and using the BD Diva acquisition software (version 9.0) analysed using FlowJo (Tree Star, version 10.8.1).

Cell death analysis

Cell death was measured using an IncuCyte imaging system, as described previously[35]. In brief, cells were imaged in the presence of the cell-impermeable DNA intercalator Sytox Green (Thermo Fisher, R37168), and Sytox-positive cells were quantified at each time point using custom processing definitions, available on request. In parallel, separate cells plated in identical numbers were treated with the cell-permeable dye Syto Green (Thermo Fisher, S34854) and quantified using the same approach, and percentage cell death was calculated as $Sytox^+/Syto^+$ at each time point. For siRNA-knockdown cell death assays, to avoid excessive non-specific toxicity, cells were transfected with siRNA for 8 h, at which point cells (adherent) were washed and dye/inhibitors were added at final concentrations immediately before IncuCyte imaging.

Pathology

Pathology analysis for the *Adar*$^{P195A/p150null}$*::Zbp1* experiments (Supplementary Fig. 2) was carried out by the same personnel and using a similar scoring system recently described for analysis of *Adar*$^{P195A/p150null}$ mice[5]. In brief, littermate mice 21 days of age were euthanized through CO_2 asphyxiation and livers and kidneys were collected and washed in PBS and fixed in 10% neutral-buffered formalin. Tissues were embedded in paraffin and cut into sections of about 4 mm in thickness for haematoxylin and eosin staining. Liver and kidney sections were also stained with periodic acid–Schiff (PAS) stain. Slides were evaluated by a board-certified veterinary pathologist, who was blinded to genotype and experimental setup. For kidney, expansion of the glomerular mesangial matrix was scored from 0–4, with 0, normal; 1, minimal; 2, mild; 3, moderate; 4, severe. For the liver, microvesicular and lesser macrovesicular cytoplasmic vacuolation were scored from 0–5, with 0, normal; 1, minimal changes affecting only a small region (<5%) of the liver; 2, mild changes throughout the liver but without enlargement of hepatocytes, coalescing lesions or necrosis; 3, mild to moderate cytoplasmic vacuolation throughout the liver with enlargement of hepatocytes but no necrosis or loss of parenchyma; 4, moderate, coalescing throughout the liver with multifocal mild regions of loss of parenchyma or necrosis; 5, severe with moderate multifocal regions of cavitation and necrosis.

Tissues for the *Adar*$^{P195A/p150null}$*::Mlkl*$^{-/-}$*::Casp8*$^{-/-}$ experiments (Supplementary Fig. 11) were collected from pups euthanized by decapitation on the day of birth, and spleen, kidney, liver, heart, head with brain, and gastrointestinal tract were routinely embedded in paraffin and stained with haematoxylin and eosin. PAS stains were also obtained for liver and kidney. These slides were reviewed blindly, with the exception of gastrointestinal tissues, for which the pathologist was not blinded to genotype.

Representative images were captured from scanned slides or from glass slides taken using NIS-Elements BR 3.2 64-bit and image plates were created in Adobe Photoshop. Image white balance, lighting and contrast were adjusted using autocorrections applied to the entire image. Original magnification is stated in the figure captions.

Analysis of IBA1 and cleaved caspase 3 for *Mlkl::Casp8::Adar*$^{p150null/P195A}$ pups was carried out through the University of Washington Histology and Imaging Core utilizing the Leica Bond Rx Automated Immunostainer (Leica Microsystems). Slides were deparaffinized with Leica Dewax solution at 72 °C for 30 s. Antigen retrieval was carried out on all slides with EDTA, pH 9, at 100 °C for 20 min. All subsequent steps were carried out at room temperature. Initial blocking consisted of 10% normal goat serum (Jackson ImmunoResearch, catalogue number 005-000-121) in Tris-buffered saline for 20 min and further blocking with Leica Bond peroxide block for 5 min. Slides were incubated with IBA1 (1:1,000) or CC3 (1:250) primary antibodies in Leica primary antibody

diluent. Slides were scanned in brightfield mode with a 20× objective using a NanoZoomer Digital Pathology System. Quantification of CC3 and IBA1 was carried out using the Visiopharm Image Analysis module.

Quantitative PCR analysis

RNA was isolated from primary MEFs or LET1 cells using Trizol extraction and first-strand cDNA synthesis was carried out with SuperScript III Reverse Transcriptase (Invitrogen, catalogue number 18080044). Quantitative PCR was carried out using a ViiA 7 Real Time PCR System (Thermo Fischer Scientific) using SYBR reagents (Thermo Fisher). The following primers were used for quantitative PCR: *Zbp1*, sense (S): 5′-AAGAGTCCCCTGCGATTATTTG-3′, antisense (AS): 5′-TCTGGATGG CGTTTGAATTGG-3′; *Ripk1*, S: 5′-GAAGACAGACCTAGACAGCGG-3′, AS: 5′-CCAGTAGCTTCACCACTCGAC-3′; *Ccl2*, S: 5′-TGGCTCAGCCAGAT GCAGT-3′, AS: 5′-TTGGGATCATCTTGCTGGTG-3′; *Ccl7*, S: 5′-CCAC ATGCTGCTATGTCAAGA-3′, AS: 5′-ACACCGACTACTGGTGATCCT-3′; *Ifit1*, S: 5′-GCCATTCAACTGTCTCCTG-3′, AS: 5′-GCTCTGTCTGTG TCATATACC-3′; *Ifnb*, S: 5′-CTGGAGCAGCTGAATGGAAAG-3′, AS: 5′-CTTCTCCGTCATCTCCATAGGG-3′; *Gapdh*, S: 5′-GGCAA ATTCAACGGCACAGT-3′, AS: 5′-AGATGGTGATGGGCTTCCC-3′.

RNA-sequencing and NanoString analysis

RNA was isolated from day-23 spleens (for RNA-seq) or treated cells (for NanoString experiments) using Trizol. An on-column DNAse treatment was included for RNA-seq experiments. Total RNA was added directly to lysis buffer from the SMART-Seq v4 Ultra Low Input RNA Kit for Sequencing (Takara), and reverse transcription was carried out followed by PCR amplification to generate full-length amplified cDNA. Sequencing libraries were constructed using the NexteraXT DNA sample preparation kit (Illumina) to generate Illumina-compatible barcoded libraries. Libraries were pooled and quantified using a Qubit Fluorometer (Life Technologies). Dual-index, single-read sequencing of pooled libraries was carried out on a HiSeq2500 sequencer (Illumina) with 58-base reads, using HiSeq v4 Cluster and SBS kits (Illumina) with a target depth of 10 million reads per sample.

For NanoString, 254 transcripts were quantified from total RNA using the mouse nCounter Inflammation V2 panel (NanoString). The nSolver Analysis Software 4.0 with the nCounter Advanced Analyses package (version 2.0.134) was used to normalize the data and perform differential gene expression analysis to generate $\log_2$[fold change] values and *P* values. Data visualizations were carried out in R (version 4.1.1). Differentially expressed genes were visualized as heatmaps and volcano plots using the packages pheatmap (version 1.0.12) and ggplot2 (version 3.3.5).

For RNA-seq analysis of day-23 spleens, reads were aligned using kallisto[36] to the mouse reference genome (GRCm39) using default parameters. Quality control was carried out on raw reads using fastqc, and raw reads were then combined with aligned reads using multiqc (ref. [37]), with no samples removed from the final dataset owing to quality control checks. Analysis of aligned reads was carried out with R using DESeq2 (ref. [38]) using standard parameters to generate differential gene expressions for each of the conditions against the WT, and significant differential expression was defined by adjusted *P* value < 0.01 and absolute $\log_2$[fold change] > 1. The differential expression data were annotated using the bioMaRt package[39,40]. Fold changes against WT mice for ADAR1-deficient ($Adar^{P195A/p150null}$) mice, with and without *Zbp1-a* knockout, were compared, defining genes with a >50% regression to a fold change of 0 after *Zbp1-a* knockout as high-recovery genes and all others as low-recovery genes. Gene ontology analysis was carried out using the clusterProfiler package[41] using standard parameters comparing both high- and low-recovery genes against background separately.

Statistical analysis

Comparison of survival curves was carried out using a log-rank (Mantel–Cox) test. *P* values less than 0.0001 were a result of the statistical analysis package performed by GraphPad Prism and are represented as $P < 0.0001$. Data shown in graphs are mean or mean ± s.d. If the data fulfilled the criteria for Gaussian distribution tested by column statistics, an unpaired parametric *t*-test with Welch's correction was carried out for statistical analysis. All statistical tests listed in the figure legends were two-sided and were carried out using Graphpad Prism, or Microsoft Excel (chi-square power values for Mendelian distributions). *P* values are presented in the figures or figure legends, generally, we used the following conventions: NS ($P > 0.05$), $^{*}P \leq 0.05$, $^{**}P \leq 0.01$, $^{***}P \leq 0.001$, $^{****}P \leq 0.0001$. All in vitro experiments, unless otherwise stated, were independently replicated a minimum of two times, and details on replication of displayed data are stated in the figure legends.

Reporting summary

Further information on research design is available in the Nature Research Reporting Summary linked to this paper.

Data availability

RNA-seq and NanoString data are available through the Gene Expression Omnibus of the National Institutes of Health, accession numbers GSE200854 (RNA-seq) and GSE200985 and GSE200986 (NanoString). Source data are provided with this paper.

Code availability

The R analysis was carried out using publicly available code, described in the Methods section; custom R scripts are available at https://github.com/OberstLab/Hubbard-et-al-2022-Nature.

27. Murphy, J. M. et al. The pseudokinase MLKL mediates necroptosis via a molecular switch mechanism. *Immunity* **39**, 443–453 (2013).
28. Kasparcova, V. et al. Cutting edge: RIP1 kinase activity is dispensable for normal development but is a key regulator of inflammation in SHARPIN-deficient mice. *Immunol.* **192**, 5476–5480 (2014).
29. Lin, J. et al. RIPK1 counteracts ZBP1-mediated necroptosis to inhibit inflammation. *Nature* **540**, 124–128 (2016).
30. Newton, K., Sun, X. & Dixit, V. M. Kinase RIP3 is dispensable for normal NF-kappa Bs, signaling by the B-cell and T-cell receptors, tumor necrosis factor receptor 1, and Toll-like receptors 2 and 4. *Mol. Cell. Biol.* **24**, 1464–1469 (2004).
31. Salmena, L. et al. Essential role for caspase 8 in T-cell homeostasis and T-cell-mediated immunity. *Gene Dev.* **17**, 883–895 (2003).
32. Henao-Mejia, J. et al. Generation of genetically modified mice using the CRISPR–Cas9 genome-editing system. *Cold Spring Harb. Protoc.* https://doi.org/10.1101/pdb.prot090704 (2016).
33. Shin, K.-J. et al. A single lentiviral vector platform for microRNA-based conditional RNA interference and coordinated transgene expression. *Proc. Natl Acad. Sci. USA* **103**, 13759–13764 (2006).
34. Zarnegar, B. J. et al. irCLIP platform for efficient characterization of protein–RNA interactions. *Nat. Methods* **13**, 489–492 (2016).
35. Orozco, S. et al. RIPK1 both positively and negatively regulates RIPK3 oligomerization and necroptosis. *Cell Death Differ.* **21**, 1511–1521 (2014).
36. Bray, N. L., Pimentel, H., Melsted, P. & Pachter, L. Near-optimal probabilistic RNA-seq quantification. *Nat. Biotechnol.* **34**, 525–527 (2016).
37. Ewels, P., Magnusson, M., Lundin, S. & Käller, M. MultiQC: summarize analysis results for multiple tools and samples in a single report. *Bioinformatics* **32**, 3047–3048 (2016).
38. Love, M. I., Huber, W. & Anders, S. Moderated estimation of fold change and dispersion for RNA-seq data with DESeq2. *Genome Biol.* **15**, 550 (2014).
39. Durinck, S. et al. BioMart and Bioconductor: a powerful link between biological databases and microarray data analysis. *Bioinformatics* **21**, 3439–3440 (2005).
40. Durinck, S., Spellman, P. T., Birney, E. & Huber, W. Mapping identifiers for the integration of genomic datasets with the R/Bioconductor package biomaRt. *Nat. Protoc.* **4**, 1184–1191 (2009).
41. Yu, G., Wang, L.-G., Han, Y. & He, Q.-Y. clusterProfiler: an R Package for comparing biological themes among gene clusters. *OMICS J. Integr. Biol.* **16**, 284–287 (2012).

Acknowledgements This work is supported by the grants R01 AI153246 (to A.O. and D.B.S.), R01 CA228098 (to A.O.), R01 AI084914 (to D.B.S.), R01 AI143227 and R01 AI147177 (to R.S.), a Titus Fellowship (to N.W.H.), T32 T32AR7108-41 (to J.M.A.), and a Helen Hay Whitney Foundation Postdoctoral Fellowship (to N.S.G.). Extended Data Fig. 9a was created with BioRender.com. We thank P. Jain, I. Silva and R. Lee for technical assistance.

Author contributions Conceptualization: N.W.H., M.M., D.B.S., A.O.; methodology: N.W.H., M.M., R.S., L.H.C., N.S.G., D.B.S., A.O.; analysis: N.W.H. (all), J.M.A. (NanoString data), K.Y.S. (RNA-seq data analysis), J.M.S. (histopathological analysis and scoring), A.O.; investigation: N.W.H. (all), J.M.A. (NanoString, tissue culture and cell death assays),

N.S.G. (Supplementary Fig. 1 co-immunoprecipitation experiments), L.H.C. (tissue culture, western blot and co-immunoprecipitation), K.L. (flow cytometry), M.W. (*Ripk3*/*Trex1*A.O.; writing original draft: N.W.H., A.O.; writing, review and editing: all authors.

Competing interests D.B.S. is a co-founder and shareholder of Danger Bio, LLC, and a scientific advisor for Related Sciences LLC. A.O. is a co-founder and shareholder of Walking Fish Therapeutics.

Additional information

Supplementary information The online version contains supplementary material available at https://doi.org/10.1038/s41586-022-04896-7.

Correspondence and requests for materials should be addressed to Andrew Oberst.

Peer review information *Nature* thanks Andreas Linkermann and the other, anonymous, reviewer(s) for their contribution to the peer review of this work. Peer reviewer reports are available.

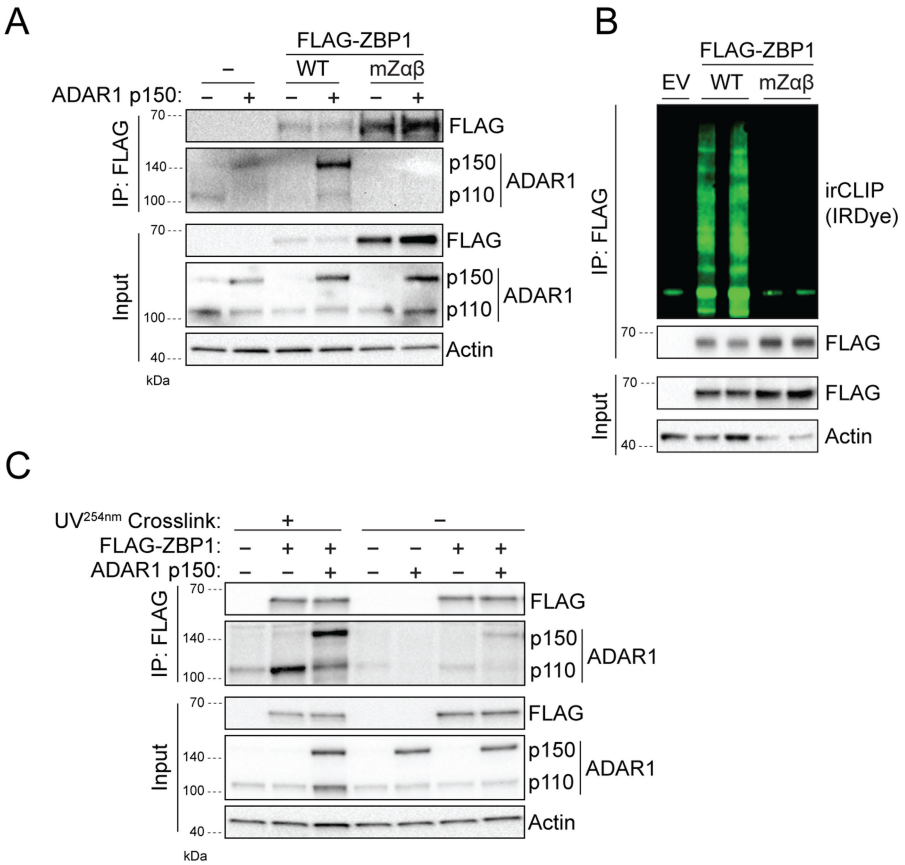

Extended Data Fig. 1 | Interaction of ZBP1 with RNA and ADAR1. **A**. Co-precipitation ADAR1 with WT or mutant Zαβ (mZαβ) Flag-tagged ZBP1 (FLAG-ZBP1) after FLAG immunoprecipitation. **B**. Immunoprecipitation and IR-CLIP analysis for RNA binding by of WT or mZαβ FLAG-ZBP1. **C**. Co-precipitation of ADAR1 and FLAG-tagged ZBP1 after UV-crosslinking. These experiments were performed in HEK293T cells.

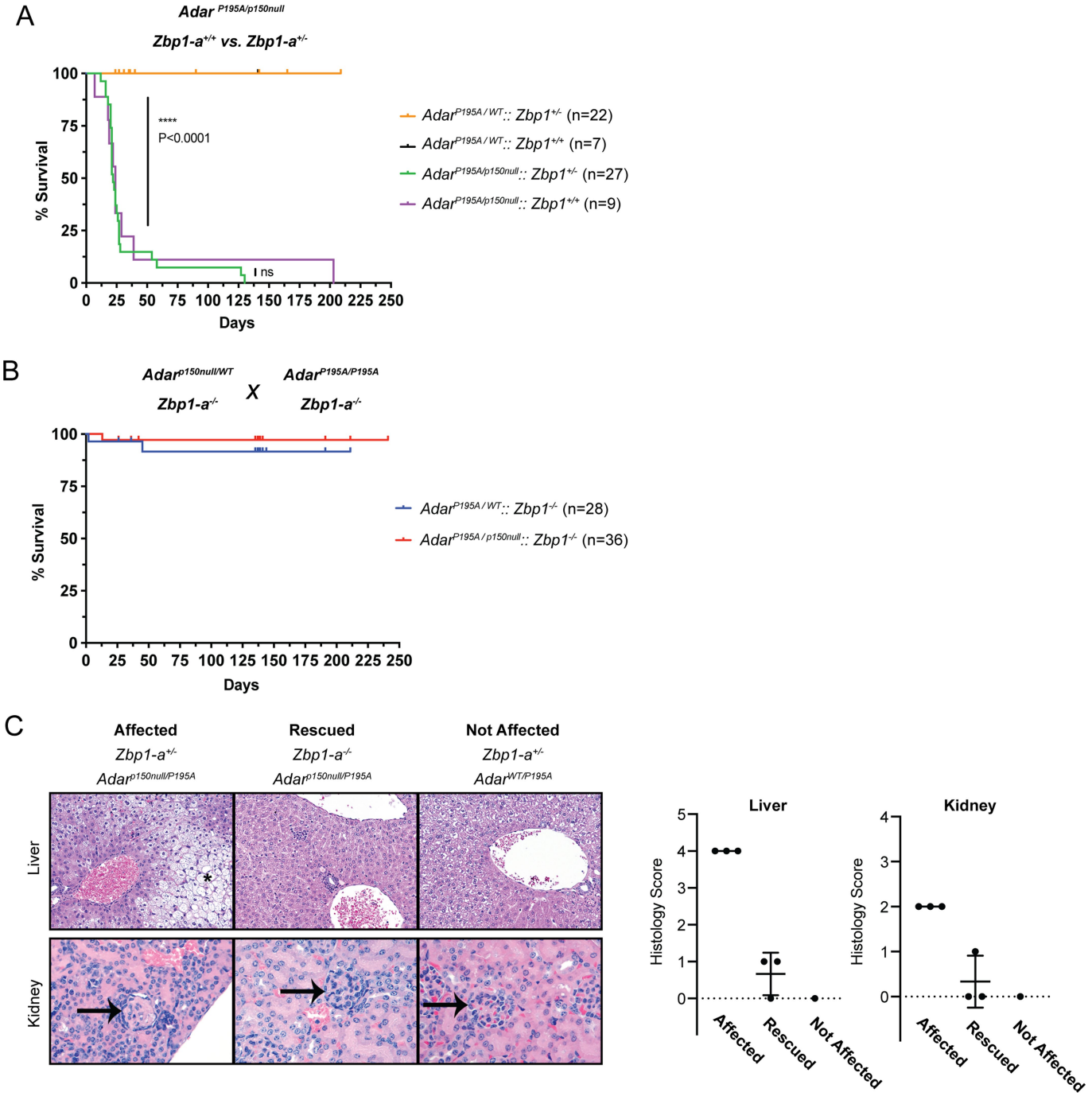

Extended Data Fig. 2 | Immunopathology in ADAR-mutant mice is ZBP1 dependent. Survival proportions observed upon cross of *Adar*$^{p150null/WT}$*::Zbp1-a*$^{+/-}$ mice to *Adar*$^{P195A/P195A}$*::Zbp1-*$^{+/-}$, **** $p < 0.0001$ (Mantel-Cox Log-Rank test) **(A)** or *Adar*$^{p150null/WT}$*::Zbp1-a*$^{-/-}$ mice to *Adar*$^{P195A/P195A}$*::Zbp1-a*$^{-/-}$, not significant (Mantel-Cox Log-Rank test) (**B**). (**C**) Histopathological analysis of liver and kidney from affected, rescued and unaffected mice (genotypes indicated.) For liver samples, regions of cytoplasmic vacuolation indicated with asterisk. Original magnification 20x, HE staining. For kidney, glomeruli are indicated with arrows, from original magnification 40x HE staining.

A

Genotype	% C57BL/6J
ZBP1-a$^{-/-}$::ADAR$^{p150null/+}$	92.56 %
ZBP1-a$^{-/-}$::ADAR$^{p150null/+}$	85.35 %
ZBP1-a$^{-/-}$::ADAR$^{P195A/P195A}$	92.03 %
ZBP1-a$^{-/-}$::ADAR$^{P195A/P195A}$	90.36 %
ZBP1-a$^{-/-}$::ADAR$^{p150nul/P195A}$	91.59 %
ZBP1-a$^{-/-}$::ADAR$^{p150nul/P195A}$	92.15 %
ZBP1-a$^{-/-}$::ADAR$^{p150nul/P195A}$	91.27 %
ZBP1-a$^{-/-}$::ADAR$^{p150nul/P195A}$	89.31 %
Control C57BL/6J	100.0 %
ZBP1-a$^{-/-}$	84.29 %
ZBP1-a$^{-/-}$	85.32 %

B

Genotype	% C57BL/6J
ZBP1-g$^{-/-}$::ADAR$^{p150null/P195A}$	98.38 %
ZBP1-g$^{-/-}$::ADAR$^{p150null/P195A}$	98.16 %
ZBP1-g$^{-/-}$::ADAR$^{P195A/P195A}$	98.13 %
ZBP1-g$^{-/-}$::ADAR$^{P195A/P195A}$	98.21 %

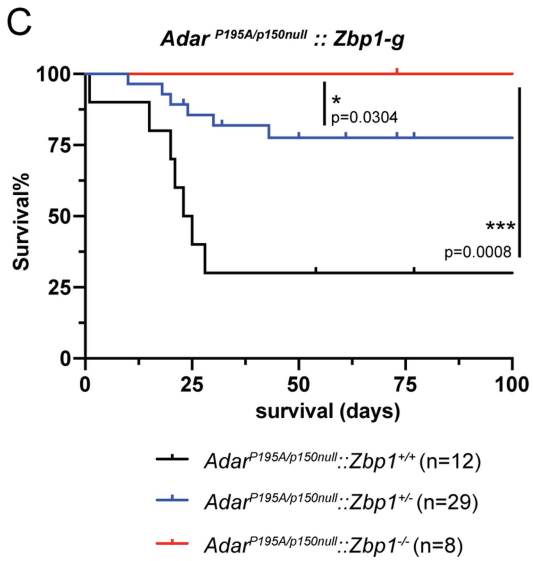

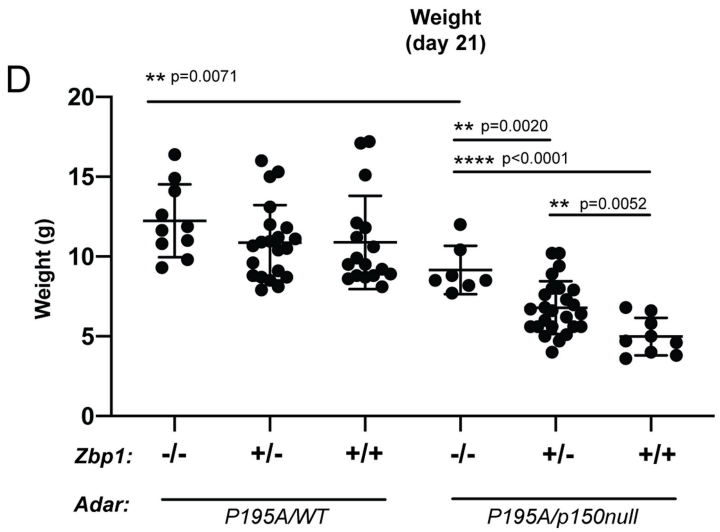

Extended Data Fig. 3 | Cross of *Adar*$^{P195A/p150null}$ mice to a separately derived, fully congenic *Zbp1*$^{-/-}$*-g* strain. A–B. SNP typing analysis of ZBP1-g **(A)** and ZBP1-a **(B)** mice. **C–D.** *Zbp1*$^{-/-}$*-g::Adar*$^{P195A/p150null}$ survival proportions(**C**) and observed weight (**D**) at 21 days (weaning). Combined male & female, Zbp1$^{+/+}$::Adar$^{P195A/WT}$ (n = 17), Zbp1$^{+/-}$::Adar$^{P195A/WT}$ (n = 21), Zbp1$^{-/-}$::Adar$^{P195A/WT}$ (n = 10), Zbp1$^{+/+}$::Adar$^{P195A/p150null}$ (n = 9), Zbp1$^{+/-}$::Adar$^{P195A/WT}$ (n = 25), Zbp1$^{-/-}$::Adar$^{P195A/WT}$ (n = 7).

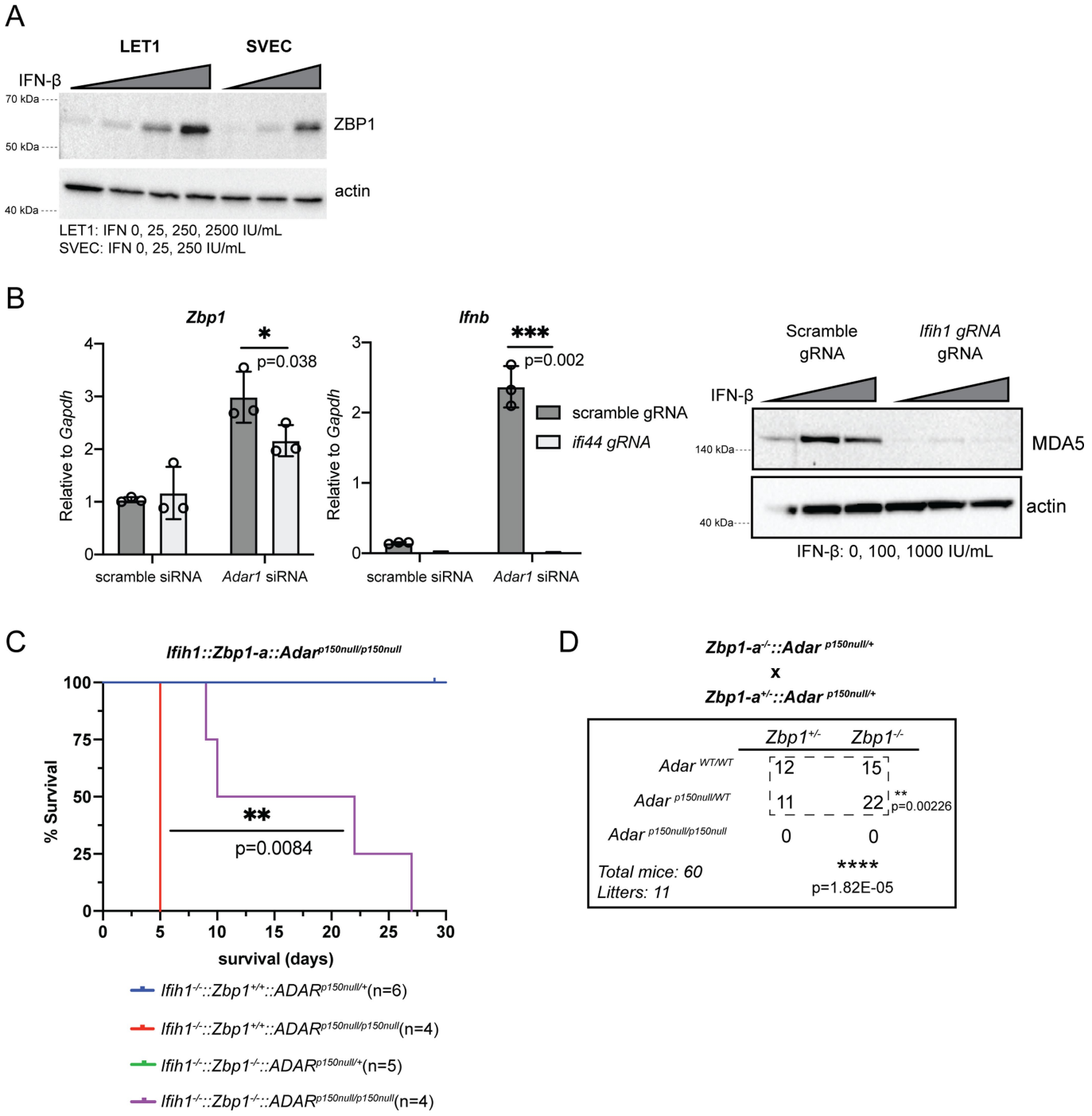

Extended Data Fig. 4 | ZBP1 is IFN dependent and partially dependent on MDA5. A. Twelve-hour stimulation of LET1 and SVEC cells with varying concentrations of IFN-β followed by Western Blot analysis for ZBP1 protein. **B**. Quantitative PCR analysis for *Zbp1* and *Ifnb* after ADAR1 depletion in wild-type (scramble gRNA) or MDA5 knockout LET1. Gene was normalized against *Gapdh*. Significance determined by individual student t-tests. Each group (*Zbp and Ifnb*) contains 3 biologic replicates, each comprising the average of 4 technical replicates). This experiment is representative of two independent repeats. Whisker bars are presented as mean +/− SD. **C**. Survival of $Zbp1^{-/-}$::$MDA5^{-/-}$::$ADAR^{p150null/p150null}$ mice. Zbp1-$a^{+/+}$::$Ifih1^{-/-}$::$Adar^{p150null/+}$ n = 6, Zbp1-$a^{+/+}$::$Ifih1^{-/-}$::$Adar^{p150null/p150null}$ n = 4, Zbp1-$a^{-/-}$::$Ifih1^{-/-}$::$Adar^{p150null/+}$ n = 5, Zbp1-$a^{-/-}$::$Ifih1^{-/-}$::$Adar^{p150null/p150null}$ n = 3. Statistical significance determined by Mantel-Cox (Log-Rank) test. **D**. Survival proportions of *$Zbp1^{-/-}$-a::$Adar^{p150/WT}$ intercross*. Chi square power analysis performed, indicating significance at $p = 1.82 \times 10^{-5}$.

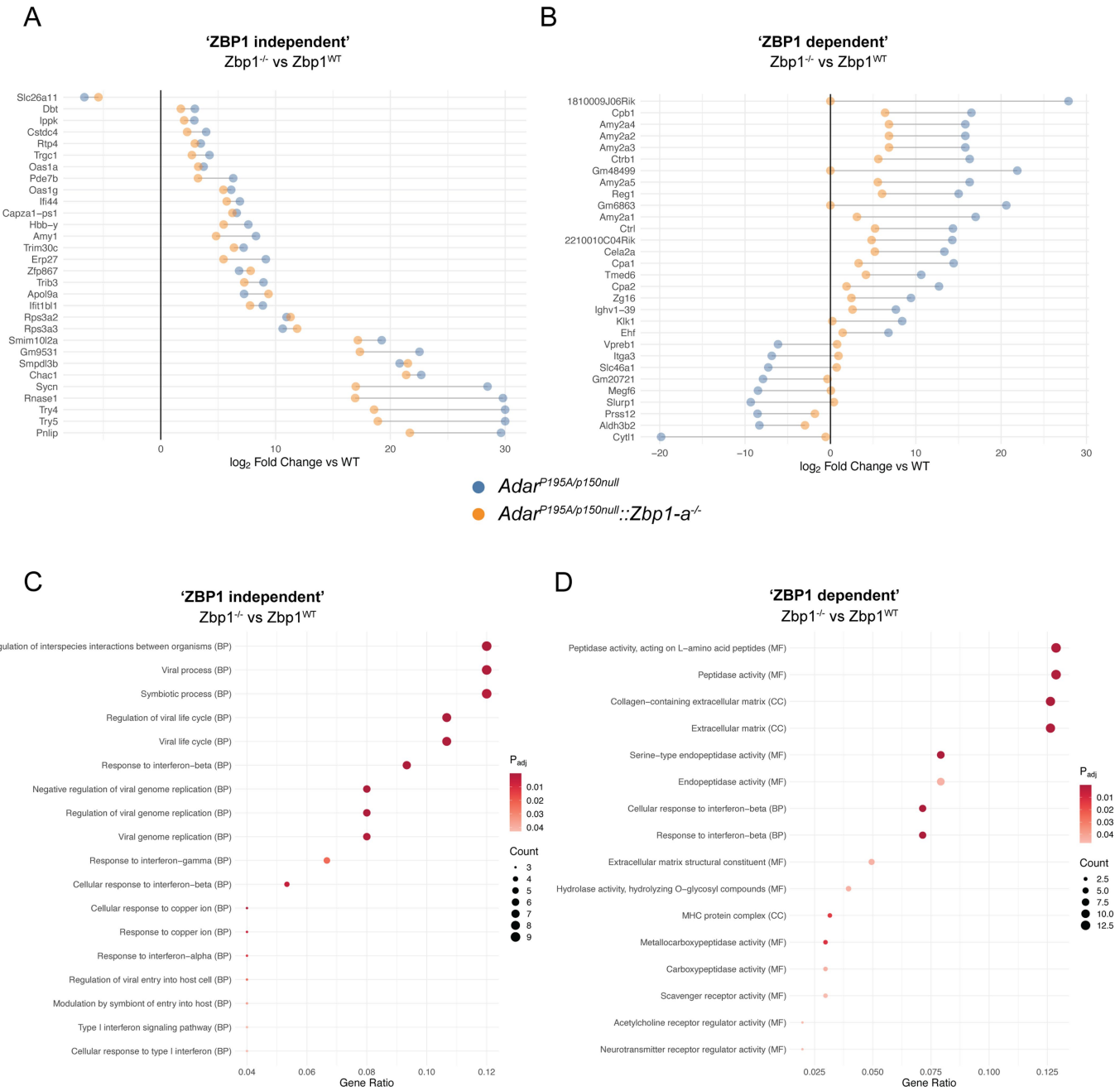

Extended Data Fig. 5 | Identification of ZBP1 dependent and independent aspects of the ADAR1 inflammatory signature. A–B: Cleveland plots indicating changes in the ADAR1 dependent gene signature observed in the spleens of 23 day old mice, indicating most- **(A)** and least- **(B)** changed genes upon ZBP1 ablation in *Adar*$^{P195A/p150null}$ mice. Gene selection is the top 30 largest contributors to the ZBP1 dependent **(A)** and independent **(B)** signature from ADAR$^{P195A/p150null}$ mice, in comparison to WT mice. Gene Ontology analysis was performed on the signatures from **A** and **B**. **C–D**: GO-terms analysis for ZBP1-independent signature **(C)**, and the ZBP1 dependent signature analysis **(D)**.

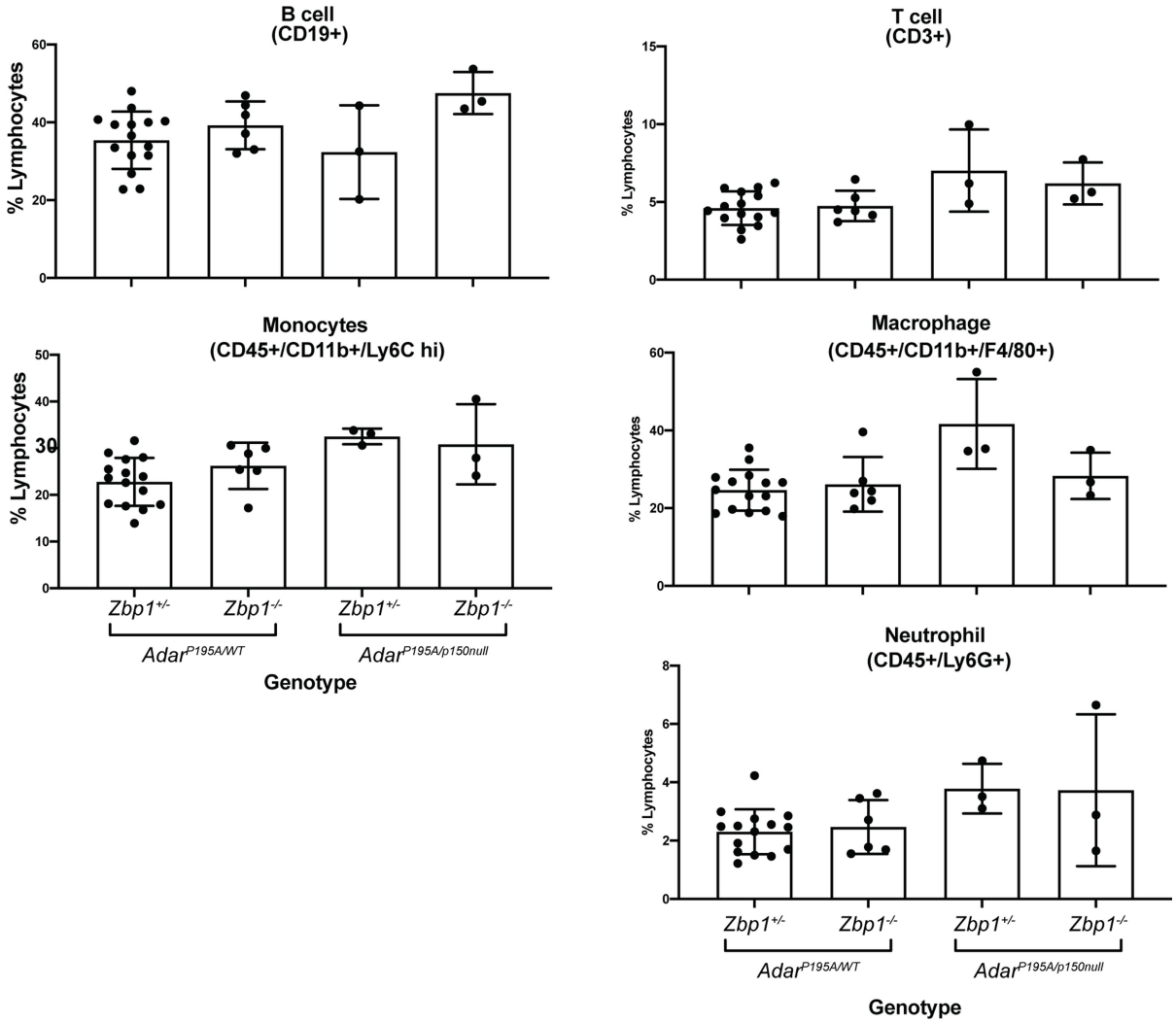

Extended Data Fig. 6 | Flow cytometry analysis of splenic cellular subsets. B cell, T cell, monocyte, macrophage percentages from day 23 spleens of *Zbp1::Adar*$^{p150/P195A}$ mice.

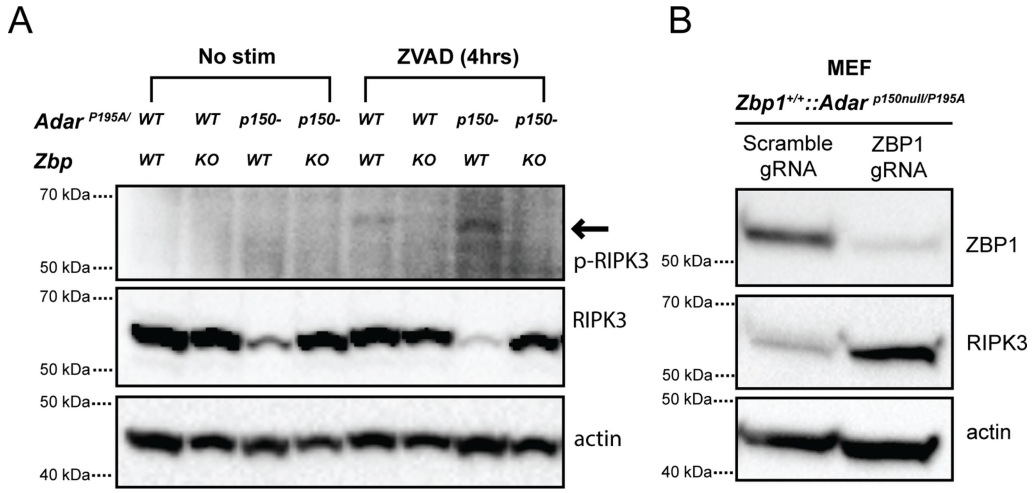

Extended Data Fig. 7 | ZVAD treatment induces phosphorylation of RIPK3 in ADAR mutant MEFs in a ZBP1 dependent fashion. A. Analysis of phospho-RIPK3 in ADAR1 mutant MEFs after 4 h ZVAD treatment. **B**. Confirmation of ZBP1 gRNA knockout in ADAR1 mutant MEFs.

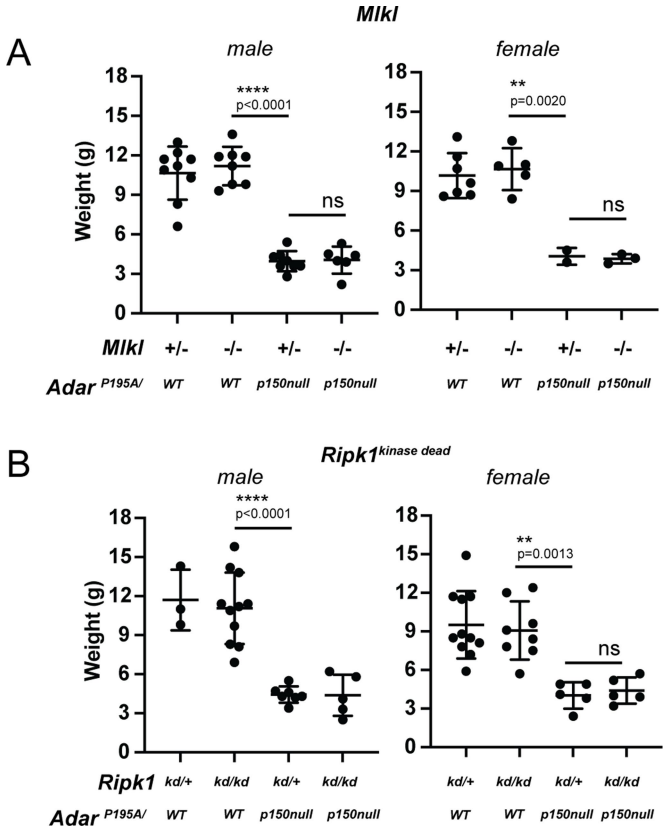

Extended Data Fig. 8 | MLKL or RIPK1$^{kinase\ dead}$ mutations do not rescue ADAR$^{P195A/p150null}$ mutation. Three-week-old weights (weaning) of male or female *Adar$^{P195A/p150null}$* mice crossed to animals lacking, **A**: MLKL. Mlkl$^{+/-}$::Adar$^{P195A/WT}$ (m/f n = 9/7), Mlkl$^{+/-}$::Adar$^{P195A/p150null}$ (m/f n = 8/2), Mlkl$^{-/-}$::Adar$^{P195A/WT}$ (m/f n = 8/5), Mlkl$^{-/-}$::Adar$^{P195A/p150null}$ (m/f n = 6/3). or **B**: carrying a point mutation abrogating the kinase activity of RIPK1 (*Ripk1^{kd}*). Ripk1$^{kd/+}$::Adar$^{P195A/WT}$ (m/f n = 3/11), Ripk1$^{kd/+}$::Adar$^{P195A/p150null}$ (m/f n = 7/5), Ripk1$^{kd/kd}$::Adar$^{P195A/WT}$ (m/f n = 11/8), Ripk1$^{kd/kd}$::Adar$^{P195A/p150null}$ (m/f n = 5/5). Statistical differences determined by individual student t-tests (two tailed). All genotypes are littermates from mixed litters.

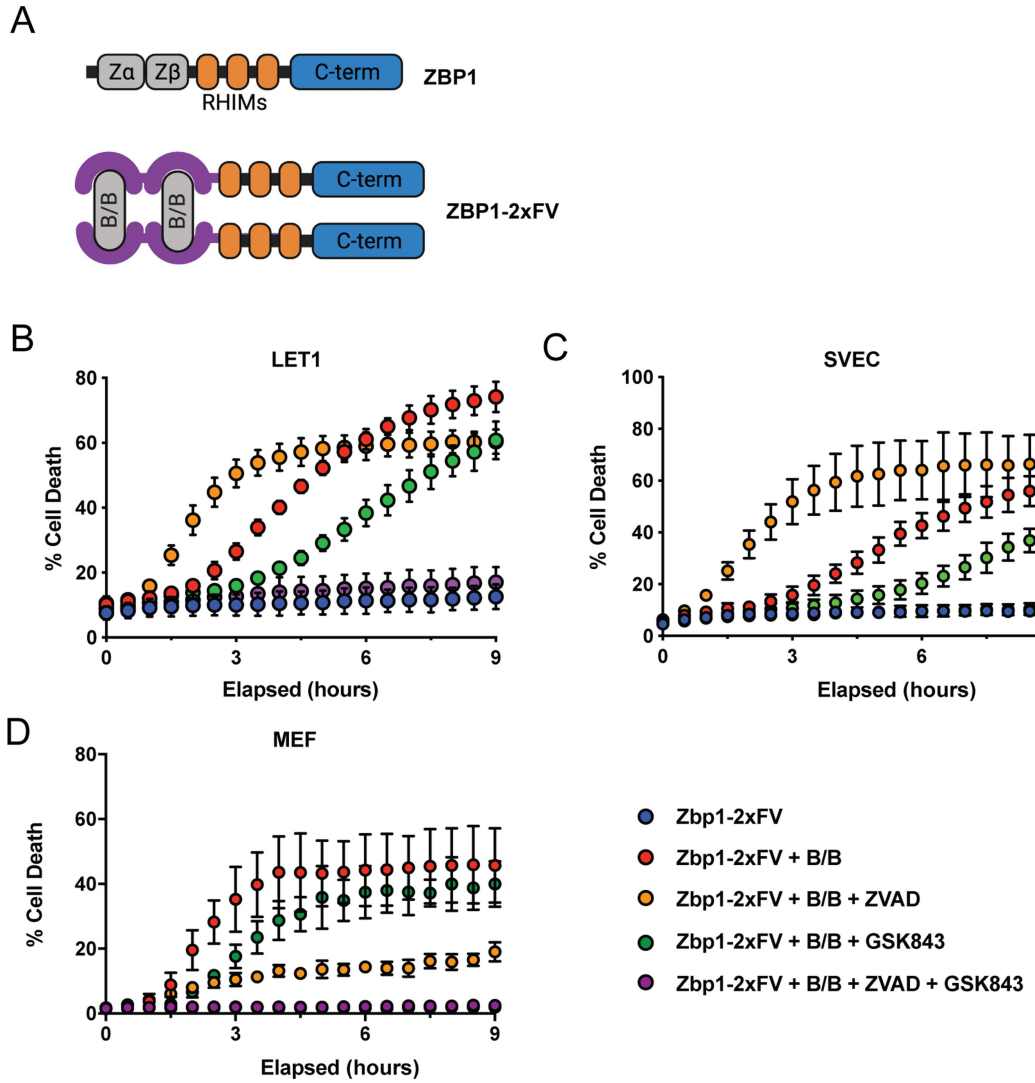

Extended Data Fig. 9 | Oligomerization of ZBP1 triggers necroptotic cell death. A. Schematic indicating the replacement of ZBP1's Z-DNA binding domain with a tandem FKBP domain. **B**–**D**: Cell death following addition of B/B homodimerizer with indicated combinations of ZVAD and GSK843 in LET1s (each group, n = 4 biologic replicates) **(B)**, SVECs (each group n = 4 biologic replicates) **(C)** or MEFs (each group n = 3 biologic replicates) **(D)**. Statistical significance was determined by unpaired t tests (two-tailed). Experiments B and C are representative of two independent experiments, and D is representative of 3 independent experiments. All whisker bars are presented as mean +/− SD.

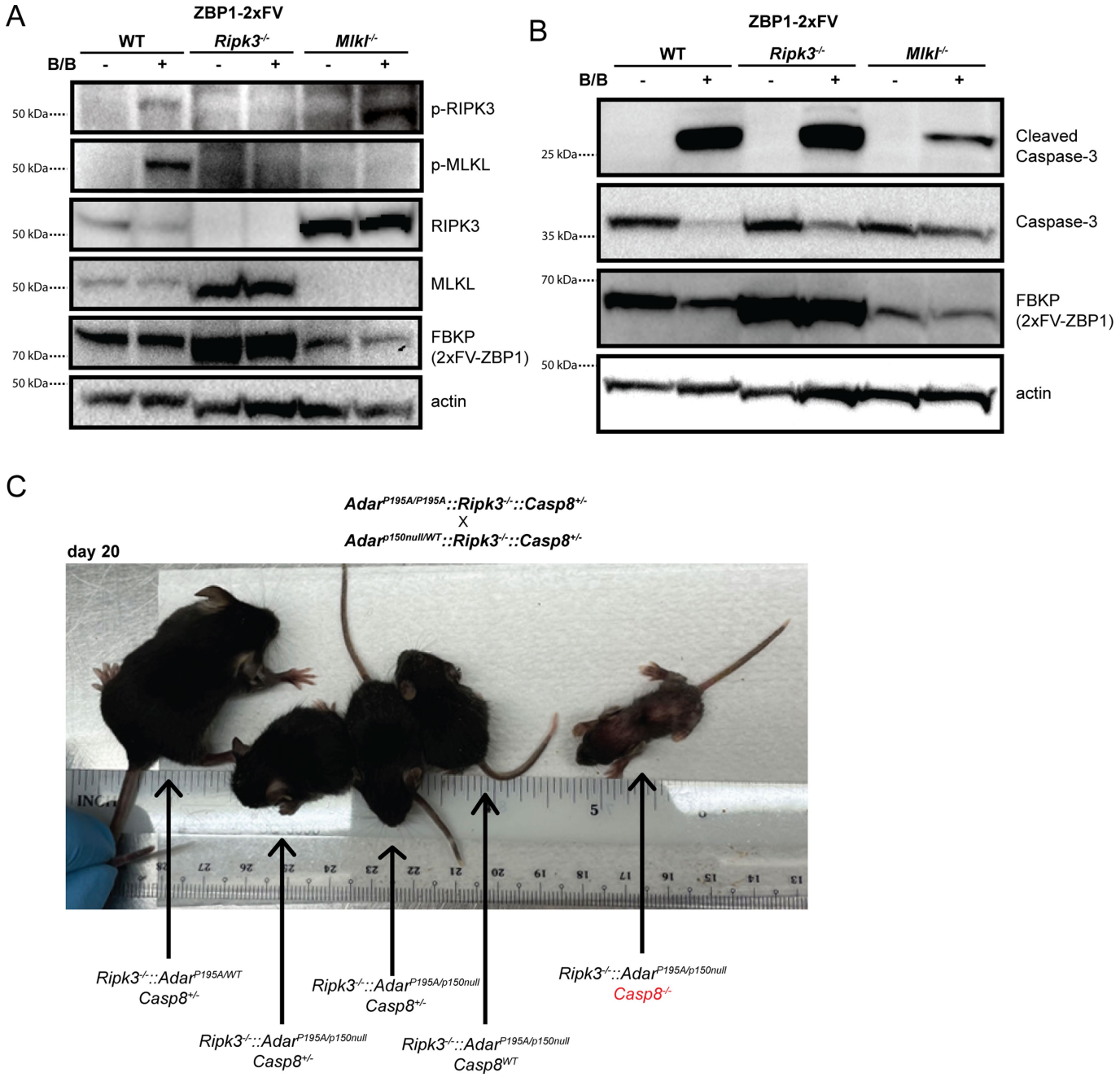

Extended Data Fig. 10 | Molecular analysis of cell death induced by ZBP1-2xFV homodimerization. A. Phospho-MLKL analysis of ZBP1-2xFV MEFs (wild-type, Ripk3$^{-/-}$, MLKL$^{-/-}$) after 1 h stimulation with B/B homodimerizer. **B**. Cleaved-caspase 3 analysis of ZBP1-2xFV MEFs (wild-type, Ripk3$^{-/-}$, MLKL$^{-/-}$) after 3 h stimulation with B/B homodimerizer. **C**. Representative image depicting Caspase-8 deficiency exacerbation of disease phenotype in ADAR$^{P195A/p150null}$::RIPK3$^{-/-}$ mice. Image of 20-day old littermates from the cross depicted in Fig. 4b.

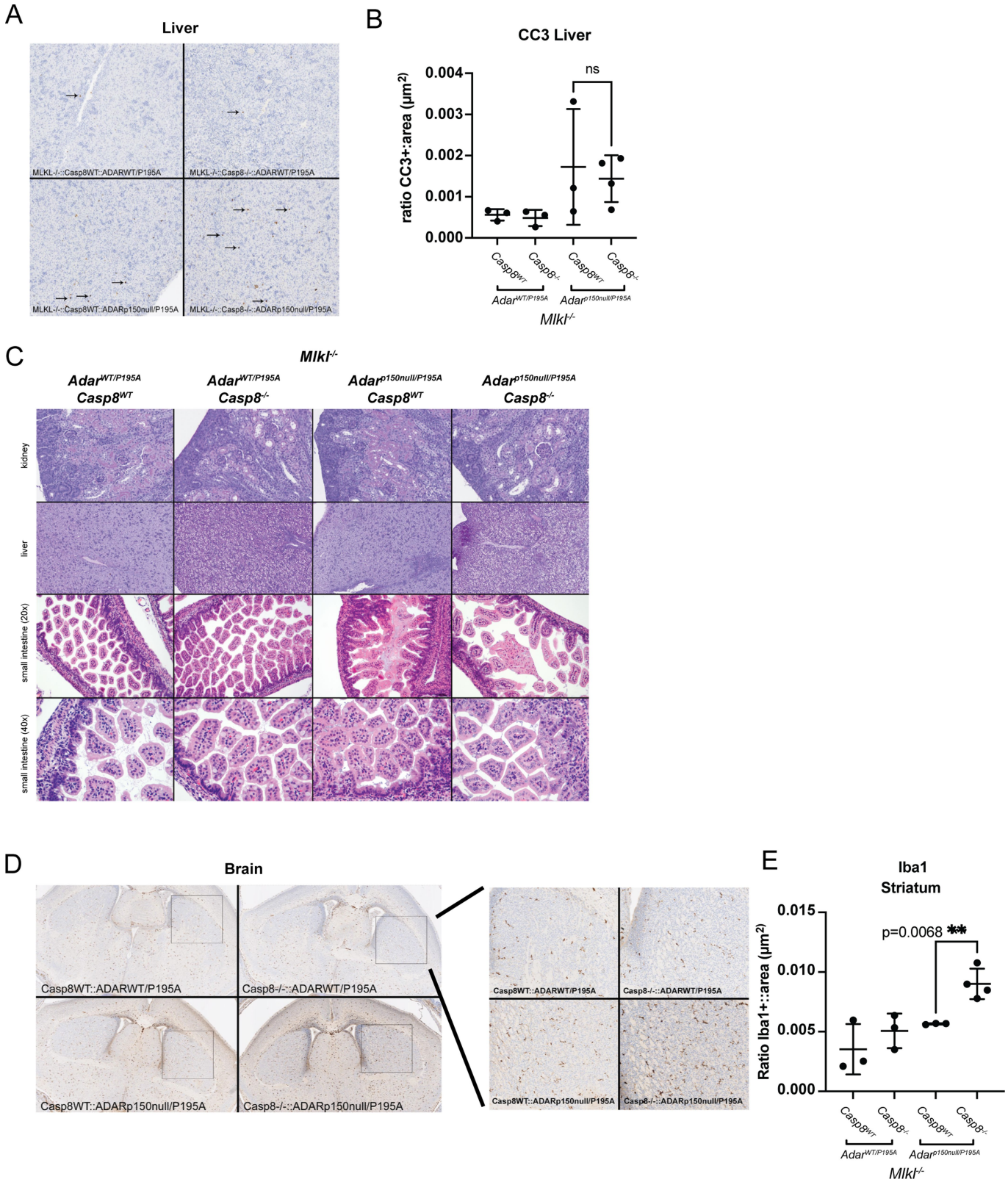

Extended Data Fig. 11 | Pathologic analysis of Mlkl$^{-/-}$::Casp8$^{-/-}$::Adar$^{p150null/P195A}$ mice. A–B. Immunohistochemical staining **(A)** and quantification **(B)** in liver for cleaved-caspase 3. (n = 3 d.0 pups, each group) Original magnification 10x. **C.** Additional histological images of other tissue sites (kidney, liver and small intestine). Kidney (20x) and liver (10x) PAS staining, small intestine HE staining (original magnification as stated). **D–E.** Immunohistochemical staining, with 2.5x and 10x images **(D)** and quantification **(E)** in brain for Iba1 (n = 3 d.0 pups, each group). **B** & **E** use tissues from matched animals.

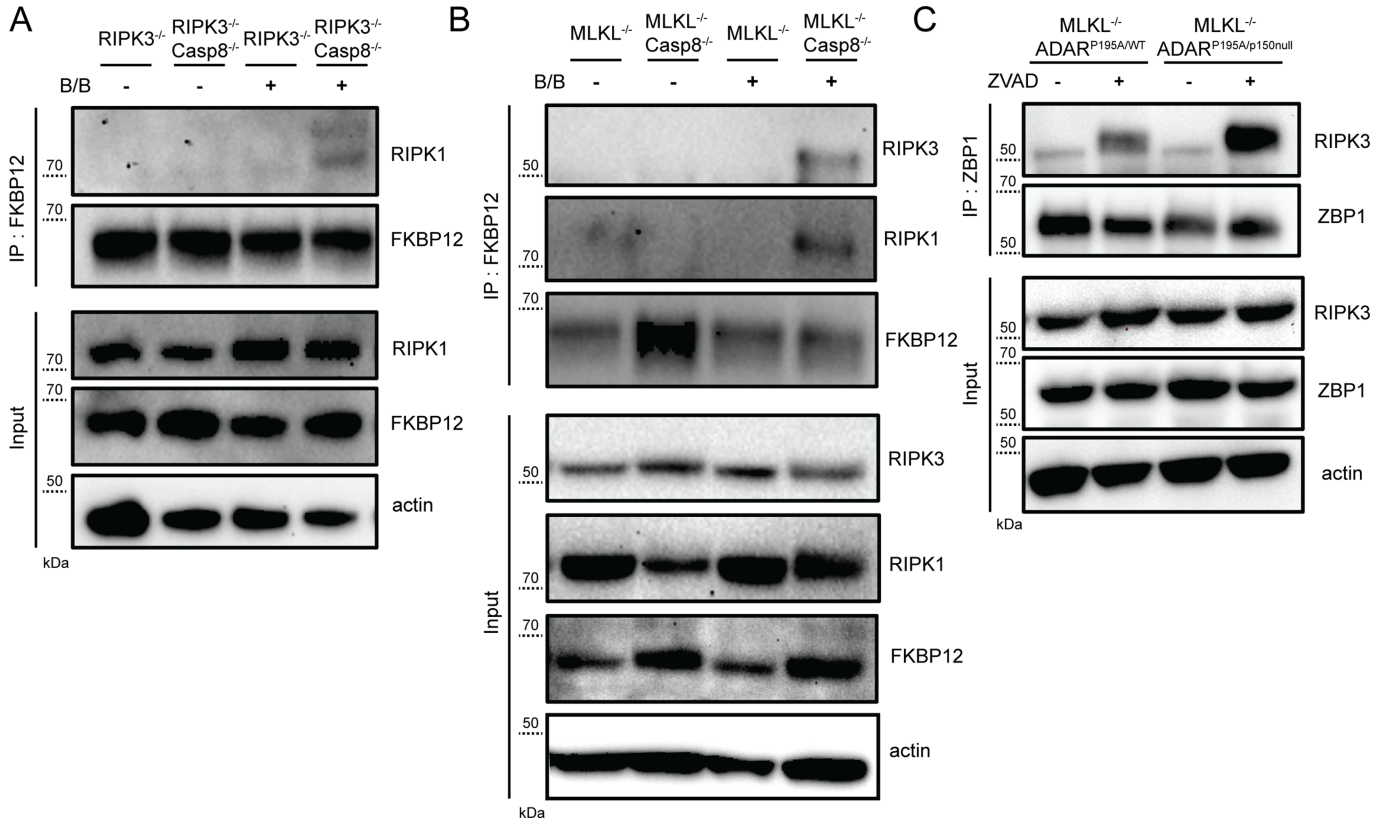

Extended Data Fig. 12 | Immunoprecipitation of RIPK3 and RIPK1 by ZBP1 is enhanced by Casp8 deficiency. A. Pulldown of ZBP1-2xFV (FKBP) and co-precipitation of RIPK1 in *Ripk3*$^{-/-}$*::Casp8*$^{-/-}$ *MEFs*. **B**. Pulldown of ZBP1-2xFV (FKBP) and co-precipitation of RIPK1 and RIPK3 in *Mkl*$^{-/-}$*::Casp8*$^{-/-}$ *MEFs*. **C**. Pulldown of ZBP1 and co-precipitation of RIPK3 and in *Mlkl*$^{-/-}$*::Adar*$^{p150null/P195A}$ *MEFs*.

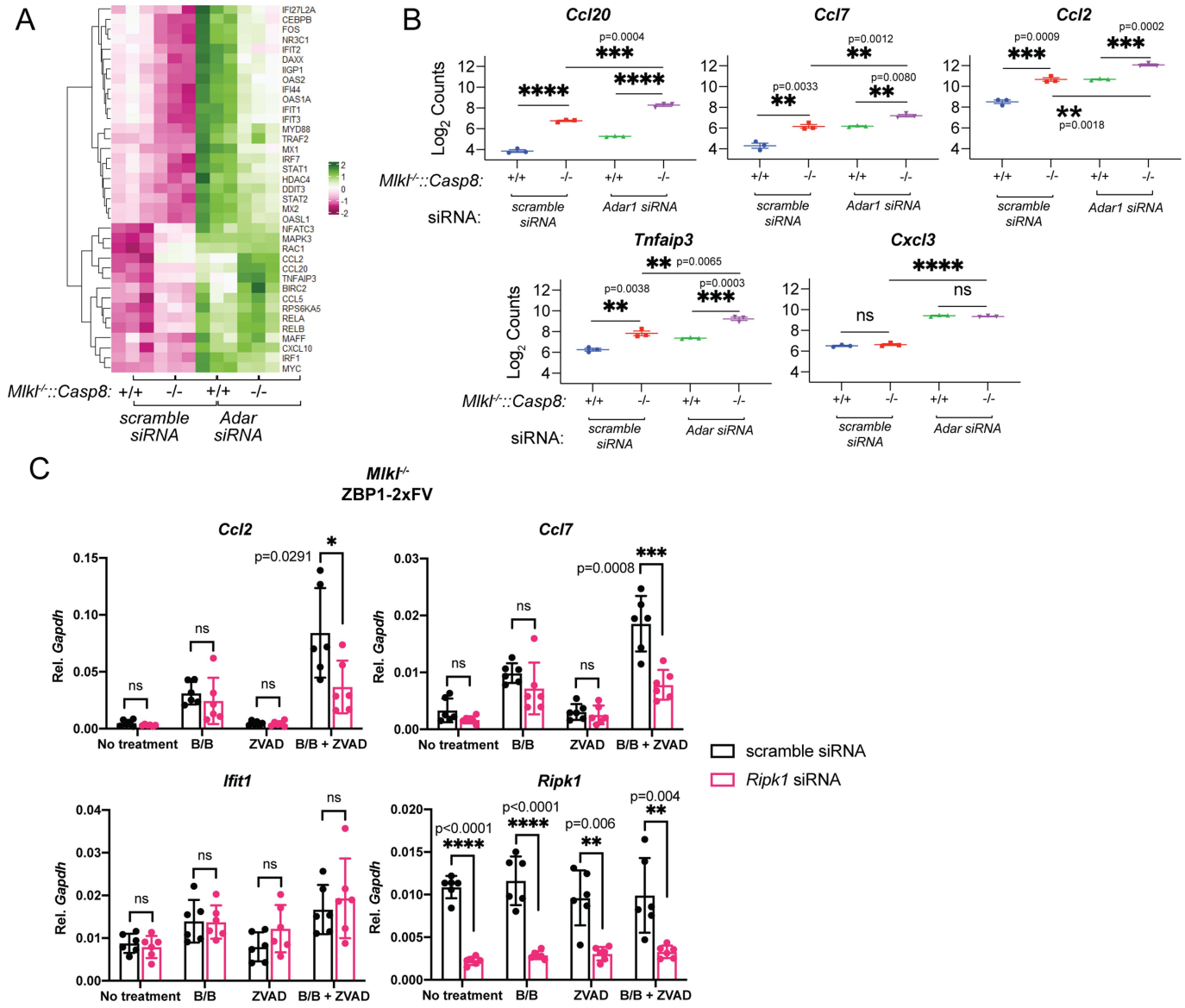

Extended Data Fig. 13 | ZBP1 activation results in RIPK1 dependent, RIPK3 independent gene transcription which is enhanced by knockout of *Casp8*. **A–B** Differential transcript analysis of *Mlkl*$^{-/-}$::Casp8$^{+/+}$ and Mlkl$^{-/-}$::Casp8$^{-/-}$ MEFs (n = 3) following ADAR depletion, by **(A)** Heatmap analysis and **(B)** individual quantification of the top 5 differentially expressed genes. Statistical significance determined by individual unpaired t tests (two-tailed). Where not indicated: **** p < 0.0001. **C.** QPCR analysis of top 5 differentially expressed genes identified (B) in MEFs expressing ZBP1-2xFV after B/B activation after depletion of RIPK1. n = 6 biologic replicates for each treatment group, each representing the average of three technical replicates. Data is compiled from two independent experiments. Statistical significance determined by individual unpaired t tests (two-tailed). Where indicated: **** p < 0.0001. Whisker bars represent the mean +/− SD.

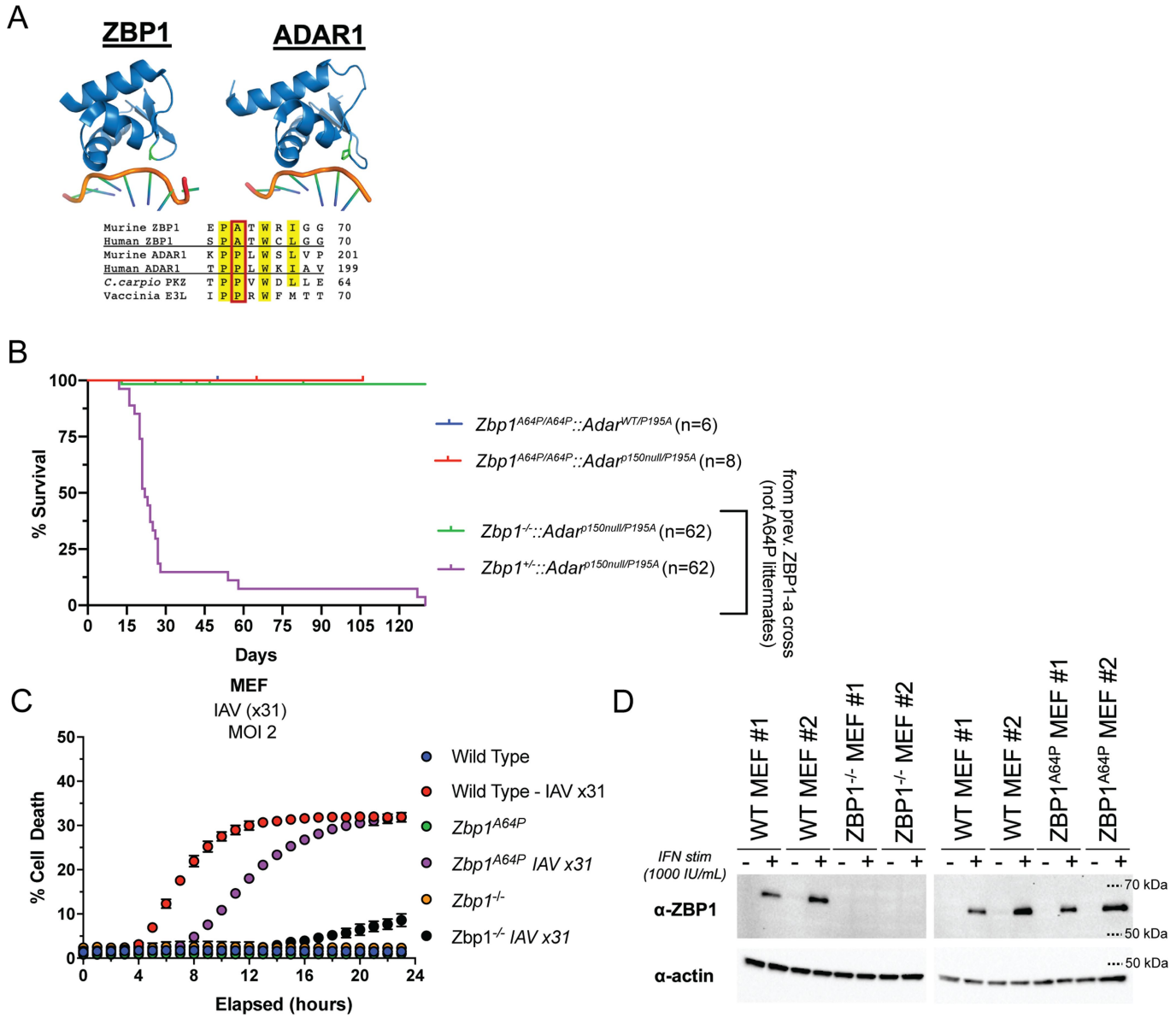

Extended Data Fig. 14 | ZBP1^{A64P} mutation attenuates ZBP1 activity in ADAR deficiency model and during influenza infection. A. Previously-reported structures of the ZBDs of ZBP1 (left) and ADAR1 (right), with A64 and P195A (respectively) highlighted in green. PDB accession #s: 1J75 and 3F21. **B**. Survival proportions of *Adar1*$^{P195A/p150null}$*::ZBP1*^{A64P} mice (n = 9 animals) compared with previous survival statistics of *Adar*$^{P195A/p150null}$*::ZBP1-a*$^{+/-}$ animals. **C**. Cell death analysis following influenza (X31, MOI 2) infection of primary MEFs derived from Wild Type (B6/J), *Zbp1*$^{-/-}$ or ZBP1$^{A64P/A64P}$ mice. Each group, n = 2 biologic replicates. Whisker bars represent the mean +/− SD. Experiment was independently replicated using MEFs derived from a different embryo. **D**. Expression of ZBP1 in wild-type, *Zbp1*$^{-/-}$, and *Zbp1*$^{A64P/A64P}$ MEFs following 24 stimulation with 1000 IU/mL murine IFN-β.

nature portfolio

Corresponding author(s): Andrew Oberst

Last updated by author(s): 04.18.2022

Reporting Summary

Nature Portfolio wishes to improve the reproducibility of the work that we publish. This form provides structure for consistency and transparency in reporting. For further information on Nature Portfolio policies, see our Editorial Policies and the Editorial Policy Checklist.

Statistics

For all statistical analyses, confirm that the following items are present in the figure legend, table legend, main text, or Methods section.

n/a	Confirmed	
☐	☒	The exact sample size (*n*) for each experimental group/condition, given as a discrete number and unit of measurement
☐	☒	A statement on whether measurements were taken from distinct samples or whether the same sample was measured repeatedly
☐	☒	The statistical test(s) used AND whether they are one- or two-sided *Only common tests should be described solely by name; describe more complex techniques in the Methods section.*
☒	☐	A description of all covariates tested
☐	☒	A description of any assumptions or corrections, such as tests of normality and adjustment for multiple comparisons
☐	☒	A full description of the statistical parameters including central tendency (e.g. means) or other basic estimates (e.g. regression coefficient) AND variation (e.g. standard deviation) or associated estimates of uncertainty (e.g. confidence intervals)
☐	☒	For null hypothesis testing, the test statistic (e.g. *F*, *t*, *r*) with confidence intervals, effect sizes, degrees of freedom and *P* value noted *Give P values as exact values whenever suitable.*
☒	☐	For Bayesian analysis, information on the choice of priors and Markov chain Monte Carlo settings
☒	☐	For hierarchical and complex designs, identification of the appropriate level for tests and full reporting of outcomes
☒	☐	Estimates of effect sizes (e.g. Cohen's *d*, Pearson's *r*), indicating how they were calculated

Our web collection on statistics for biologists contains articles on many of the points above.

Software and code

Policy information about availability of computer code

Data collection

Cell death assay data was collected by using an IncuCyte Zoom (Essen Biosciences). QPCR data was collected by using ViiA 7 Real-Time PCR System (Applied Biosystems).

Flow cytometry was performed on a BD FACSymphony A3 Cell Analyzer and using the BD Diva acquisition software (version 9.0)

Data analysis

Statistical tests not pertaining to RNAseq or nanostring analysis were performed using Graphpad Prism (version 9), or Microsoft Excel (Chi-Square Power values for mendelian distributions). All t-tests listed in the figure legends were unpaired and two-sided, with exact P values presented in the figure or figure legends.

For Nanostring, two hundred fifty-four transcripts were quantified from total RNA using the nCounter Inflammation panel. The nSolver Analysis Software 4.0 with the nCounter Advanced Analyses package (Version 2.0.134) was used to normalize the data and perform differential gene expression analysis to generate log2-fold-change values and p-values. Data visualizations were carried out in R (version 4.1.1). Differentially expressed genes were visualized as heatmaps and volcano plots using the packages “pheatmap” (version 1.0.12), and “ggplot2” (version 3.3.5).

All custom code used in these studies is available here: https://github.com/OberstLab/Hubbard-et-al-2022-Nature

For RNA seq analysis of day 23 spleens, reads were aligned using kallisto35 to the mouse reference genome (GRCm39) using default parameters. Quality control was performed on raw reads using fastqc and then combined with aligned reads using multiqc36, with no samples excluded from the final dataset due to QC checks. Analysis of aligned read was performed with R using DESeq237 using standard parameters to generate differential gene expressions for each of the conditions against wild type, and significant differential expression was defined by adjust P-value < 0.01 and absolute log2 fold change > 1. The differential expression data was annotated using the bioMaRt package38,39. Fold changes against wild-type between ADAR1 depletion, with and without Zbp1-a knockout were compared, defining high recovery genes as those with a >50% regression to a fold change of 0 after Zbp1-a knockout and as low recovery otherwise. Gene ontology analysis was

performed using the clusterProfiler package40 using standard parameters comparing both high and low recovery genes against background separately.

Flow cytometry data was analyzed using FlowJo (Tree Star, version 10.8.1). GraphPad Prism version 9 was used for generation of plots and statistical analysis, and microsoft excel was used for Chi-squared analysis and basic data management.

For manuscripts utilizing custom algorithms or software that are central to the research but not yet described in published literature, software must be made available to editors and reviewers. We strongly encourage code deposition in a community repository (e.g. GitHub). See the Nature Portfolio guidelines for submitting code & software for further information.

Data

Policy information about availability of data

All manuscripts must include a data availability statement. This statement should provide the following information, where applicable:

- Accession codes, unique identifiers, or web links for publicly available datasets
- A description of any restrictions on data availability
- For clinical datasets or third party data, please ensure that the statement adheres to our policy

The R analysis was performed using publicly available code, described above. RNAseq and Nanostring data are available via the NIH Gene Expression Omnibus, accession numbers GSE200854 (RNAseq) and GSE200985 and GSE200986 (NanoString).

Field-specific reporting

Please select the one below that is the best fit for your research. If you are not sure, read the appropriate sections before making your selection.

☒ Life sciences ☐ Behavioural & social sciences ☐ Ecological, evolutionary & environmental sciences

For a reference copy of the document with all sections, see nature.com/documents/nr-reporting-summary-flat.pdf

Life sciences study design

All studies must disclose on these points even when the disclosure is negative.

Sample size	Due to unpredictable factors when initiating these studies, primarily unknown disease severity and unknown median survival time of each genotype within the survival experiments, no statistical methods were used to predetermine sample size. Instead, survival curves and animal health were monitored at an ongoing basis until it was possible to determine when statistical significance (or insignificance) had been adequately achieved.
Data exclusions	No data exclusions were made.
Replication	All mouse crosses and survival curves were performed using at least three separate breeders, and where possible, the male and female in the breeder pair was alternated for the ADAR p150 and ADAR P195A alleles. In each of these mouse studies, all attempts at replication were successful. For all in vitro studies, we independently replicated each experiment at least three times (biological replicates). For cell death assays, a minimum of two technical replicates were used, each representing at least 4 images/well. RNAseq analysis was performed using a minimum of four biologic replicates (day 23 spleens) sampled from three litters.
Randomization	The experiments were not randomized. Randomization within mouse survival studies was not necessary as mice were not subjected to any variable treatment groups, they were solely compared based on their survival and phenotype within litter groups.
Blinding	Pathology was performed on blinded sample sets. Otherwise, investigators were not blinded to allocations during experiments and outcome assessment, as no major perturbations were performed and results were based on passive observation. Sample selection for RNAseq and nanostring datasets was performed on a 'first-come-first-serve' basis, where samples were selected based on the order in which the required genotypes arose (taking place over the course of several litters from different breeders).

Reporting for specific materials, systems and methods

We require information from authors about some types of materials, experimental systems and methods used in many studies. Here, indicate whether each material, system or method listed is relevant to your study. If you are not sure if a list item applies to your research, read the appropriate section before selecting a response.

Materials & experimental systems

n/a	Involved in the study
☐	☒ Antibodies
☐	☒ Eukaryotic cell lines
☒	☐ Palaeontology and archaeology
☐	☒ Animals and other organisms
☒	☐ Human research participants
☒	☐ Clinical data
☒	☐ Dual use research of concern

Methods

n/a	Involved in the study
☒	☐ ChIP-seq
☐	☒ Flow cytometry
☒	☐ MRI-based neuroimaging

Antibodies

Antibodies used

Unless otherwise stated, all the following Western Blot or IHC antibodies were used at a concentration of 1:10,000.

ADAR1 (15.8.6) SantaCruz cat. no. 73408 - used at 1:100 dilution, ZBP1 (Zippy-1) AdipoGen Cat. No. AG-20B-0010-C100 (used at 1:1000), actin (C4) Millipore cat. no. MAB1501 (used at 1:50,000), MDA5 (D74E4) Cell Signaling Technologies cat. no. 5321S. Iba1 (Cat no. 019-19741) Wako-Chem, Cleaved Caspase 3 (Clone D3E9) Cell Signaling Technologies. p-RIPK3 (GEN135-35-9), Genentech (1:5000), RIPK3 (1G6.1.4) Genentech, or RIPK3 (2283) ProSci, p-MLKL (D6E3G) Cell Signaling Technologies, MLKL (MABC604) Millipore, Caspase-3 (9662) Cell Signaling Technologies, Cleaved Capsase-3 (9661) Cell Signaling Technologies, RIPK1 (38/RIP) BD Biosciences, anti-FLAG (M2) Sigma (IP, used at 1 ug/50 uL of Dynabeads), anti-FKBP12, Thermo Fisher (PA1-026A).

All the following fluorescently labeled antibodies used for flow cytometry were used at a concentration of 1:200.

FITC anti-CD19 (clone 1D3; BD Biosciences) PerCP-Cy5.5 anti-CD3e (clone 145-2C11; BD Biosciences), PE-Cy7 anti-Ly6C (clone HK1.4; Biolegend), APC anti-F4/80 (clone BM8; eBioscience), AF700 anti-Ly6G (clone 1A8; Biolegend), APC-Cy7 anti-NK1.1 (clone PK136; BD Biosciences), BV510 anti-CD8a (clone 53-6.7; BD Biosciences); BV605 anti-CD4 (clone RM4-5; BD Biosciences), BV650 anti-CD11b (clone M1/70; Biolegend), and BUV395 anti-CD45.2 (clone 104; BD Biosciences).

Validation

ADAR1 antibody was independently validated in HEK293Ts by over expression of a recombinant murine p150 ADAR1 isoform, as well as by ADAR1 depletion by siRNA treatment. ZBP1 and MDA5 antibodies were independently validated by CRISPR/Cas9 knockout of ZBP1 in LET1 and SVEC cells (murine) in combination with recombinant IFN stimulation to trigger upregulation. FKBP12 antibody was validated by doxycycline inducible expression (pSLIK vector) of a recombinant ZBP1 (sequence validated) in LET1 cells.

Iba1 and Cleaved Caspase-3 antibodies used in IHC studies were independently validated by a UW pathology core, and are routinely QC'd. (http://www.uwhistologyandimaging.org/optimized-antibodies/)

RIPK3, pRIPK3, MLKL and pMLKL antibodies were validated by staining of murine derived RIPK3 or MLKL knockout MEF lines stimulated with TNF/ZVAD. Additionally, these antibodies, in addition to RIPK1 antibody have been previously described in Newton et. al, Nature, 2016. Caspase 3 and Cleaved Caspase 3 antibodies have been previously described and validated in numerous studies, which are cited and available on the manufacturers website, respectively: https://www.cellsignal.com/products/primary-antibodies/caspase-3-antibody/9662 and https://www.cellsignal.com/products/primary-antibodies/cleaved-caspase-3-asp175-antibody/9661?site-search-type=Products&N=4294956287&Ntt=%289661%29&fromPage=plp&_requestid=5495504.

The flow panel and gating scheme used is was adapted from a previously validated in Akilesh et al. Science. 2019. No new antibodies were used in this panel.

Eukaryotic cell lines

Policy information about cell lines

Cell line source(s)

Primary cells (mouse embryonic fibroblasts) derived from the mice. Immortalized mouse embryonic fibroblasts were obtained by retroviral transformation of wild type primary mouse embryonic fibroblasts with the large T-antigen.

Lung Epithelial Type 1 (LET1) cells were obtained from the Aderam lab, and as previously described, were generated from lung cells isolated from C57BL/6 wild type mice

SVEC4-10 and HEK293T cells were obtained from ATCC.

Authentication

Mouse embryonic cells were genotyped by PCR typing at the time they were derived. Furthermore, all cell lines used in cell death studies (immortalized or primary) were tested for cell death competence following isolation and culture by stimulation with TNF/ZVAD (RIPK3/RIPK3 dependent death) or IAV infection (ZBP1 dependent death), and analyzed for cell death by incucyte.

LET1, SVEC4-10 and HEK293T cells were not validated. Each are commonly used cell lines and were obtained from reputable sources (LET1's from the Aderam lab - original publisher of their generation, or ATCC for HEK293Ts and SVECs)

Mycoplasma contamination	All cells and cell lines were routinely tested for mycoplasma contamination on a monthly basis. Throughout the course of these studies, no mycoplasma contamination was observed.
Commonly misidentified lines (See ICLAC register)	No ICLAC lines were used.

Animals and other organisms

Policy information about studies involving animals; ARRIVE guidelines recommended for reporting animal research

Laboratory animals	All mice (Mus musculus) were maintained on a C57BL/6N genetic background. Male and female mice used were, Zbp1-a (Ishii, K. J. et al. Nature 2008), Zbp1-g (. Newton, K. et al. Nature 2016), AdarP195A/p150null (Maurano, M. et al. Immunity 2021), Mlkl (Murphy, J. M. et al. Immunity 2013), Ripk1kd (Kasparcova, V. et al. JI Cutting Edge 2014), Ripk1mutRHIM (Lin, J. et al. Nature 2016), Ripk3(Newton, K., Sun, X. & Dixit, V. M. Mol and Cell Biol 2004), Casp8 (Oberst, A. et al. Nature 2011), Trex1 (Morita et al. Mol Cell Biol. 2004), Ifih1(Mda5) mice (Pestal et al., 2015), Zbp1A64P (here). Throughout these studies, although it was noted throughout data acquisition, no sex of mouse was used preferentially for any experiments performed in these studies, primarily due to the nature passive observation for data collection for most experiments. In some instances (mice used at early time points, or mice found dead), no sex determination was practically possible.
Wild animals	The study did not involve wild animals.
Field-collected samples	The study did not involve field-collected samples.
Ethics oversight	All animals used were cared for and used in experiments approved by the University of Washington Institutional Animal Care and Use Committee (under protocol 4298-01) in an Association for Assessment and Accreditation of Laboratory Animal Care (AAALAC)-accredited facility in accordance with the Guide for the Care and Use of Laboratory Animals and applicable laws and regulations.

Note that full information on the approval of the study protocol must also be provided in the manuscript.

Flow Cytometry

Plots

Confirm that:

☒ The axis labels state the marker and fluorochrome used (e.g. CD4-FITC).

☒ The axis scales are clearly visible. Include numbers along axes only for bottom left plot of group (a 'group' is an analysis of identical markers).

☒ All plots are contour plots with outliers or pseudocolor plots.

☒ A numerical value for number of cells or percentage (with statistics) is provided.

Methodology

Sample preparation	Single cell suspensions of dpleens for day 23 mice were harvested by mechanical lysis through a 70 uM cell strainer. Red blood cells were lysed by a 5 minute incubation in a hypotonic solution.
Instrument	Data acquisition was performed on a BD Symphony A3 is equipped with 5 lasers; 488nm blue laser, 561 nm yellow/green laser, 637nm red laser, 405nm violet laser, and 350nm UV laser.
Software	The BD Aria software was used collection and subsequent analysis was done with FlowJo version 10.
Cell population abundance	No sorting was performed.
Gating strategy	An initial FSC/SSC gate was initially used to broadly obtain lymphocyte and myeloid subsets, and a subsequent FSC-W parameter was used to gate in single cells. Subsequent gating is indicated on each data panel.

☒ Tick this box to confirm that a figure exemplifying the gating strategy is provided in the Supplementary Information.